Solar Forecasting with All-Sky-Imagers
SolFaSi

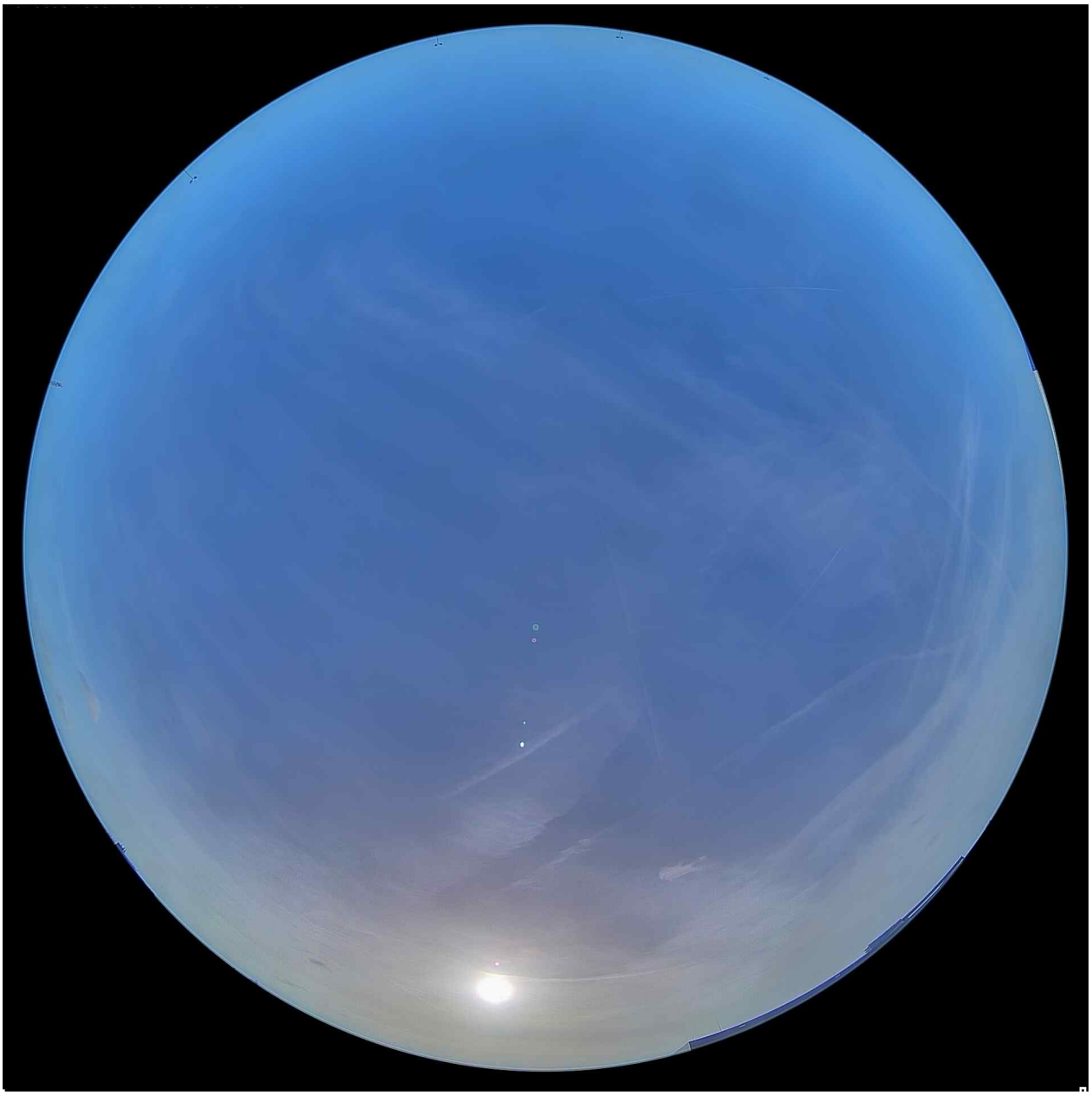

Final report

Project details

Projectnumber:	TEUE 1821406
Project title:	Solar Forecasting with All-Sky-Imagers
Coordinator:	Universiteit Utrecht
Partners:	EKO, WeDriveSolar, KNMI (subcontract UU)
Project period:	1 May 2020 – 31 October 2023

Contact details

This report is created by the project partners: Utrecht University, EKO and WeDriveSolar. For questions regarding the project, results, and follow-up projects you can contact:

Universiteit Utrecht
Wilfried van Sark
+31 30 2537611
w.g.j.h.m.vansark@uu.nl

Authors

Wilfried van Sark, Khadija Barhmi, Sara Golroodbari (UU), Wouter Knap (KNMI), Mario Pó (EKO), Robin Berg (WeDriveSolar)

Subsidy

The project was supported with a subsidy from the Dutch Ministry of Economic Affairs, National EZ subsidies, Topsector Energie, performed by the Rijksdienst voor Ondernemend Nederland (RVO).

Acknowledgements

We would like to explicitly like to thank: Marcel van Maarseveen, Arjan van Eijk, Maurits Uffing (UU), Anne van Dijke (Kadans).

Cover

The picture on the cover is taken by one of the all-sky imagers at UU on 24 January 2024.

Summary

As the number of photovoltaic (PV) systems in the Netherlands has increased fast and will continue to increase, fluctuations due to passing clouds may cause large power flow fluctuations in the electricity network. To support proper grid management in the already congested grid, an accurate PV power forecast is necessary at a high temporal and spatial resolution.

The objective of this project was to investigate how a set of all-sky imagers, also know as cloud cameras, can be used to analyse cloud movement and to predict how these clouds will move at future time horizons up to one hour, in order to forecast the power generated by solar PV systems on the ground.

Three all-sky imagers have been installed at the UU campus. One all-sky imager has been installed at KNMI, where cloud height can be calibrated with an existing ceilometer. Algorithms for the detection of clouds and analysis their movement have been developed, based on various machine learning approaches. Using stereographic analyses, cloud base heights have been determined. This allowed to construct a shadow map on the ground, which has been validated using irradiance data for UU campus.

A forecast method has been developed using machine learning, i.e., the long short-term memory neural network method performed best, although more tests are needed regarding different weather conditions with different cloud fractions.

Preface

This final report describes the work performed in the project SolFaSi (Solar Forecasting with All-Sky-Imagers, project number TEUE 1821406) as carried out within the framework of the Nationale regelingen EZ-subsidies, Topsector Energie, executed by the Rijksdienst voor Ondernemend Nederland. The report addresses the results obtained. In addition, several project changes, mostly due to the Covid pandemic, are described.

Contents

1. Introduction

Traditionally, the electricity network has been organized in a top-down fashion in which energy is produced centrally and then cascades down towards various well-defined groups of end-users. However, with the ongoing energy transition this relatively straightforward organization is changing drastically, and the complexity of control is increasing. New and more diverse assets, including photovoltaic (PV) solar energy systems, wind turbines, biogas, electric vehicles, heat pumps, and combined heat and power units (CHPs), are playing an increasingly prominent role in the energy mix. The intermittency of, and stochastic fluctuations in, the production of especially solar and wind pose new and considerable challenges for the adequate control of network power flows and quality. In addition, these new assets are also often characterized by various degrees of decentralization, thus leading to a transformation of the traditional electricity grid into a dynamic network of heterogeneous assets loosely organized in microgrids of interacting prosumers.

Ubiquitous and affordable sensor and communication technology are increasingly being used in daily life. This allows for gathering large amounts of data that provide insight in the evolution of electricity demand and supply and therewith enable for better planning and matching. In line with the present organization of the electricity market, power forecasts need to be made one day ahead while imbalances are settled on the day on a 15-minute basis. Program responsible parties (PRPs) use forecasts of electricity demand, based on weather forecasts, and manage their assets accordingly. With increasing penetration of distributed assets, in particular PV systems, on the distribution grid, these forecasts need to be adapted to compensate for local generation. At the end of 2023 a cumulative total of 24.4 GWp of PV capacity has been installed [1], about half of that in residential areas. With the plans described in the “Roadmap PV systems and Applications” a 10 times increase is foreseen by 2050 [2]. Also, already now local grid congestion is forcing network operators to disallow new grid connections and utilities to charge PV system owners in residential areas for grid feed-in, as a result of the decision not to abolish net-metering.

On the low-voltage grid level, high penetration of PV poses congestion problems, and distribution system operators (DSOs) will need additional means to guarantee security of supply

at all times of the year. A high temporal and spatial resolution forecast is needed to allow proper control of the grid. In combination with increasing (local) demand for electrified heating and electric mobility, local grid management can only be properly done using accurate forecast of supply (PV) and demand. Noteworthy, highly accurate forecasts of short-term local PV-power generation may enable higher PV penetration by employing short-term flexibility options while saving investments in grid-infrastructure and limit the need for PV curtailment. For example, studies in the USA and the Netherlands on the effect of solar forecasting for high PV penetration has shown that accurate forecasts may reduce flexibility reserves requirements in energy imbalance markets by about 20% [3] and that the potential of active power curtailment, grid reinforcement and supercapacitors to prevent or mitigate voltage fluctuations are increased with accurate forecasting [4].

Several solar forecasting methods exist, i.e., based on numerical weather predictions, statistical learning, satellite imaging and all-sky imaging. The practical use of these methods ranges from meters to kilometers and from seconds to months [5], see Figure 1. For forecast time horizons up to 30 minutes *and* spatial resolution of 1-200 meters, all-sky imaging is identified as the preferred method [6].

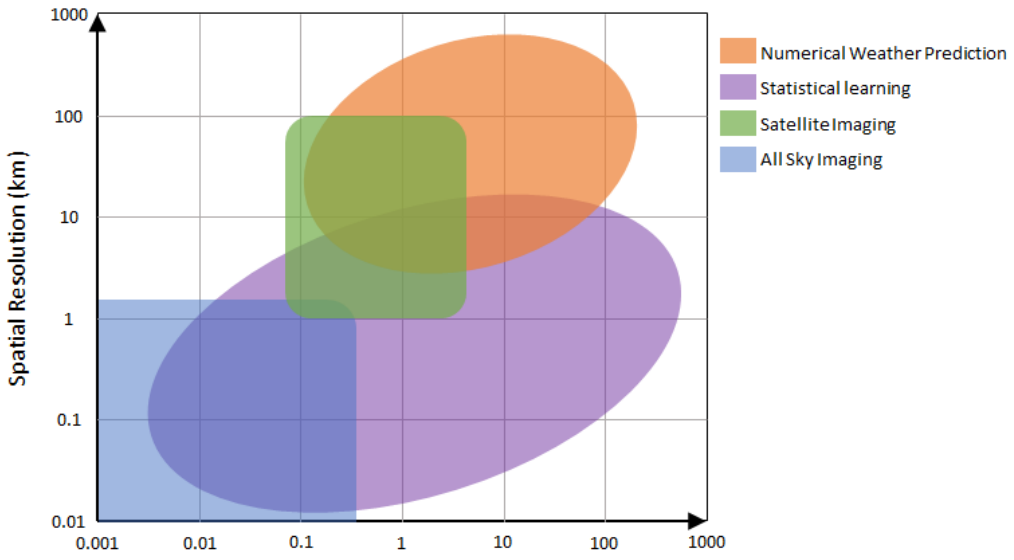

Figure 1. Overview of solar forecasting methods and their spatial and temporal horizons [5].

In all-sky imaging a wide-angle (180°) camera, usually referred to as sky camera or all-sky-imager (ASI), takes pictures of the sky which are analyzed to identify clouds. An example is shown in Figure 2 of six images taken 10 minutes apart by an ASI on the roof of one of the UU campus buildings. From analysis of such series of pictures, cloud motion vectors can be inferred, which are used to predict the future cloud cover and ground irradiance. Cloud classification schemes have been derived to account for the different cloud optical thicknesses (COTs) that affect the ground solar irradiance, e.g.: shading by thin clouds (low COT) leads to higher ground irradiance than shading by thick clouds (high COT) [7,8].

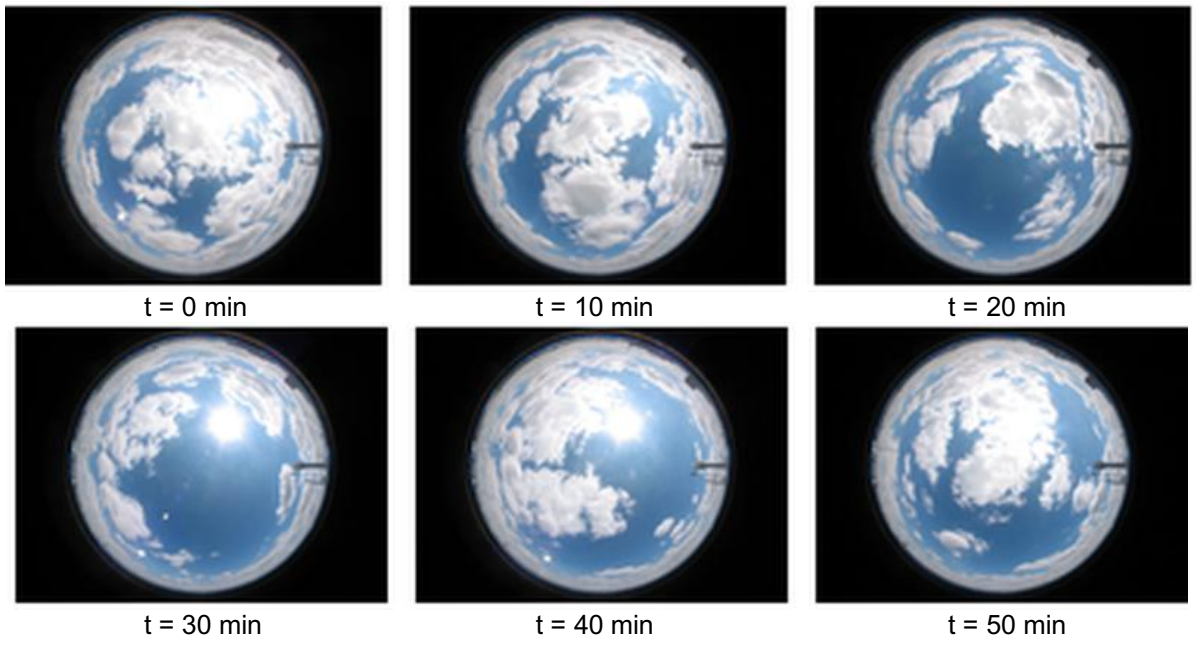

Figure 2. Example of six sky camera images at 10-minute interval illustrating the dynamical behaviour of clouds. Images have been taken on 2 July 2014 at Utrecht Science Park.

2. Goal and purpose

The goal of this project was to **develop an accurate PV power forecast method at high time resolution and high spatial resolution using a small network of all-sky imagers**. From sequences of images, the movement of clouds in the sky is followed and algorithms will be developed to predict cloud movement in the future.

A small network of four all-sky imagers has been set-up at UU campus and KNMI (see Figure 3) to allow stereoscopic analysis of cloud movement and to derive a moving shadow field, using machine learning techniques [9,10]. We planned to correlate this shadow field with the power generated by the 4000 PV modules at the UU campus buildings (blue rectangles in Figure 3).

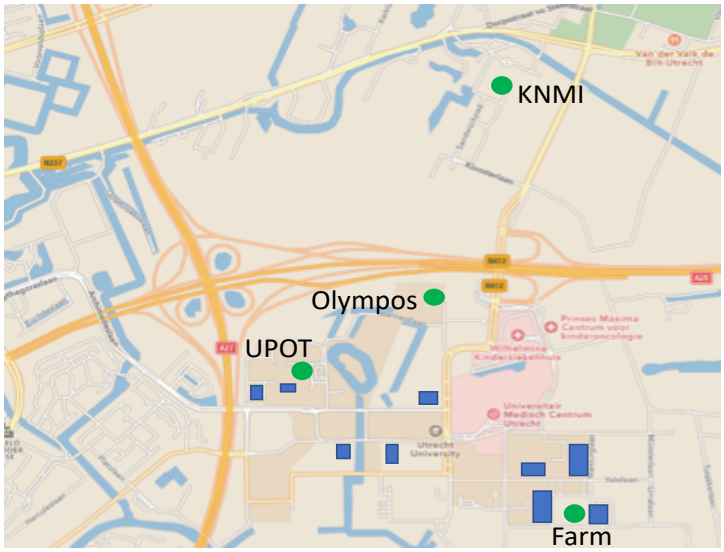

Figure 3. Planned locations of 4 all-sky imagers at UU campus (UPOT, Olympos, Farm) and KNMI. PV systems at UU campus (1.2 MWp in total) are indicated by the blue rectangles.

The accuracy of the developed forecasting methods is assessed by using several metrics, such as relative root-mean-square-error (rRMSE) and forecast skill (FS) [11]. Target values were rRMSE < 10% and FS >20%. The forecast skill is a metric that describes how a forecast method is performing with respect to persistence-based forecast, in which the irradiance (or PV power) at a certain point in time in the future is identical to the irradiance (PV power) measured or determined at a certain time t=0. If FS is larger than 0, the forecast method under study performs better than persistence.

3. Results

3.1. Setting up the imager network

This section involves the deployment of an All-Sky camera network set up at three locations at UU campus combined with one at KNMI to capture cloud movements at locations shown in Figure 4. Here the setup of the network is described, including the individual structural support systems, and data acquisition scheme that includes the KNMI camera's contributions.

Four high-end CMS-Schreder ASI-16/50 cameras supplied by EKO are installed. The precise coordinates of these locations are 52°06'04"N 5°10'40"E (De Bilt site), 52°05'16"N 5°10'03"E (Freudenthalgebouw UU), 52°05'25"N 5°10'43"E (Accelerator Building UU[1]), and 52°04'53"N 5°11'09"E (Tolakker Building, Farm), all within a maximum distance of 1.2 km from each other as seen in Figure 4.

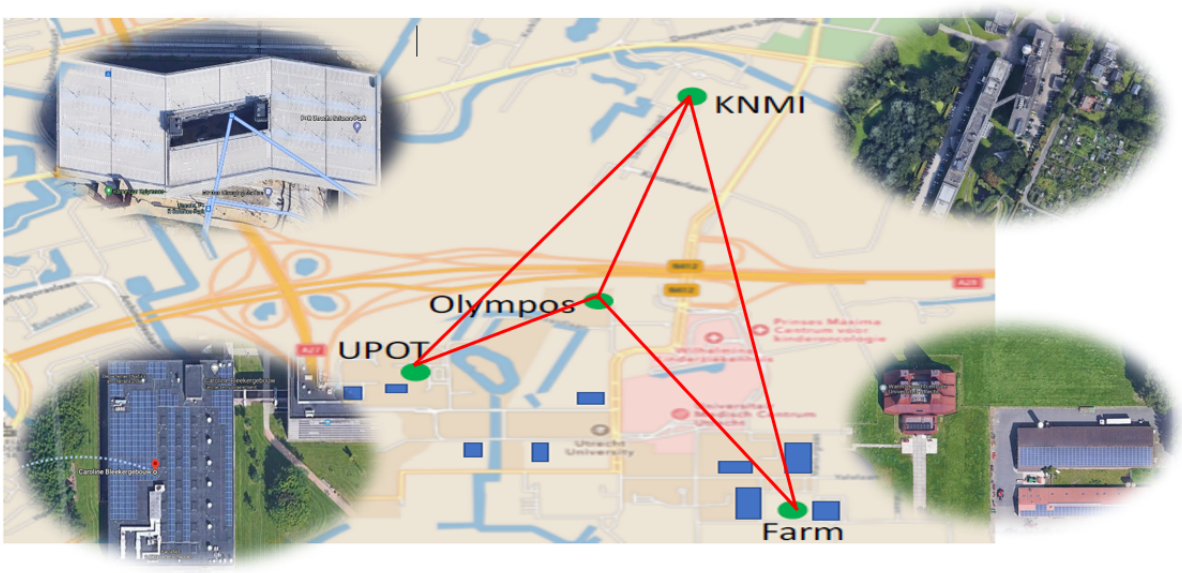

Figure 4: Google Maps view of the All-Sky cameras network located east of The City of Utrecht, The Netherlands.

In a collaborative effort with technical support staff from UU's Earth Simulation Laboratory (ESL), each camera was installed with a custom-designed support structure (see Figure 5),

[1] Note: the Olympos location was not found suitable due to newly built high buildings that would cast too much shade on the camera's. The nearby Accelerator building, owned by Kadans, allowed us to install an ASI on their roof.

Figure 5. Different Customized structures for installing the ASIs at different locations and their preparations. (A) Structure Type 1 hangs over a pole at the Freudenthal building. (B) Structure Type 2, using a solid base, this type of structure is used for The Accelerator building, (C) Similar to structure Type 1, this is located at KNMI, De Bilt, The Netherlands. (D) Preparation Phase: Showcasing the installation process with the UU installation team from the Earth Science Laboratory (ESL).

ensuring stability and optimal functioning in different settings. A thorough search for the best locations on various buildings was performed ensuring each camara could be securely mounted to withstand various environmental conditions like wind and rain. We paid careful attention to factors like temperature, humidity, and the direction of the sun and wind, thus minimizing any

potential shadows on the cameras. The effectiveness of these installations can be seen in Figure 5, which illustrates the robust and well-considered setup.

After the installation of the camera a networking process is needed to generate a virtual private network (VPN) to securely transfer data to UU data servers. Data collection was set at 15 second time resolution, leadiing to about 1000 images collected per day. This requires a large data storage system, which was organized with support from the ICT department of the Faculty of Geosciences. Also KNMI data is shared to this data storage system. A diagram illustrating the data flow of the sky camera network is presented in Figure 6.

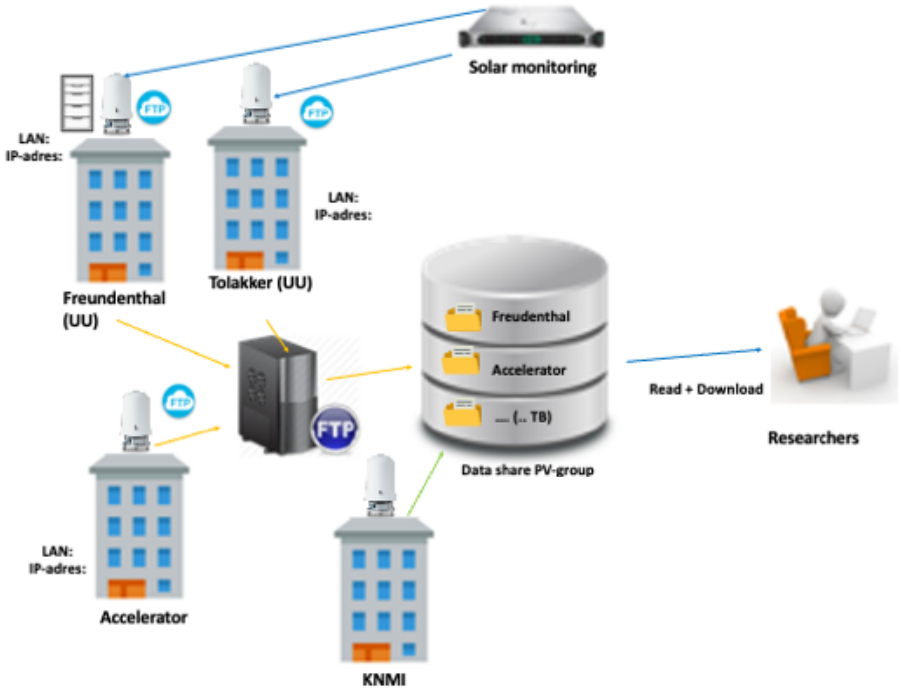

Figure 6. Diagram of data acquisition from different sky imagers.

A detailed explanation of the various components and their interconnections in the data acquasition set-up is given below:

Sky-cameras: There are several buildings, each labeled with "LAN: IP-address:" and equipped with sky cameras connected to them. These buildings are named:

- Accelerator (at UU campus)
- Freudenthal (UU)

- The Tolakker (UU)
- KNMI

FTP Servers: Each sky camera is connected to an FTP (File Transfer Protocol) server, indicated by the FTP icon. These servers are responsible for receiving data from the sky cameras.
Central Storage: There is a central storage server (also indicated with an FTP icon) which seems to be the repository for all the data coming from individual FTP servers.
Data Share PV-group: From the central storage, there is a link to a data share for the UU-PV-group (which likely stands for Photovoltaics group), indicating a shared resource for data collected from the sky cameras.
Researchers: The flow of information leads to researchers who have the ability to read and download the data from the central storage.
Solar Monitoring: In addition to the skycameras, there is a separate system for solar monitoring, with a separate IP address provided.
KNMI: At the bottom right of the image, there is a label for KNMI, which signifies that this institution is overseeing its own data flow, but also shares the data to the UU network.
The diagram in Figure 6 effectively shows how data is collected from a Network of sky cameras located on different buildings, consolidated, and then made available for analysis. Each component's role is clearly marked, with arrows indicating the direction of data flow. This setup would typically be used for comprehensive monitoring and analysis of sky and weather conditions.

The sky images constitute frames extracted from video recordings conducted during daylight hours (6:00 AM to 8:00 PM). These recordings were captured using a 5MP CMOS camera (1 x 1.8") equipped with a 360-degree fish-eye lens. The camera settings were maintained constant, including aperture, white balance, and dynamic range. Each image was captured with a resolution of 1920 x 1920 pixels, at 15-second intervals.

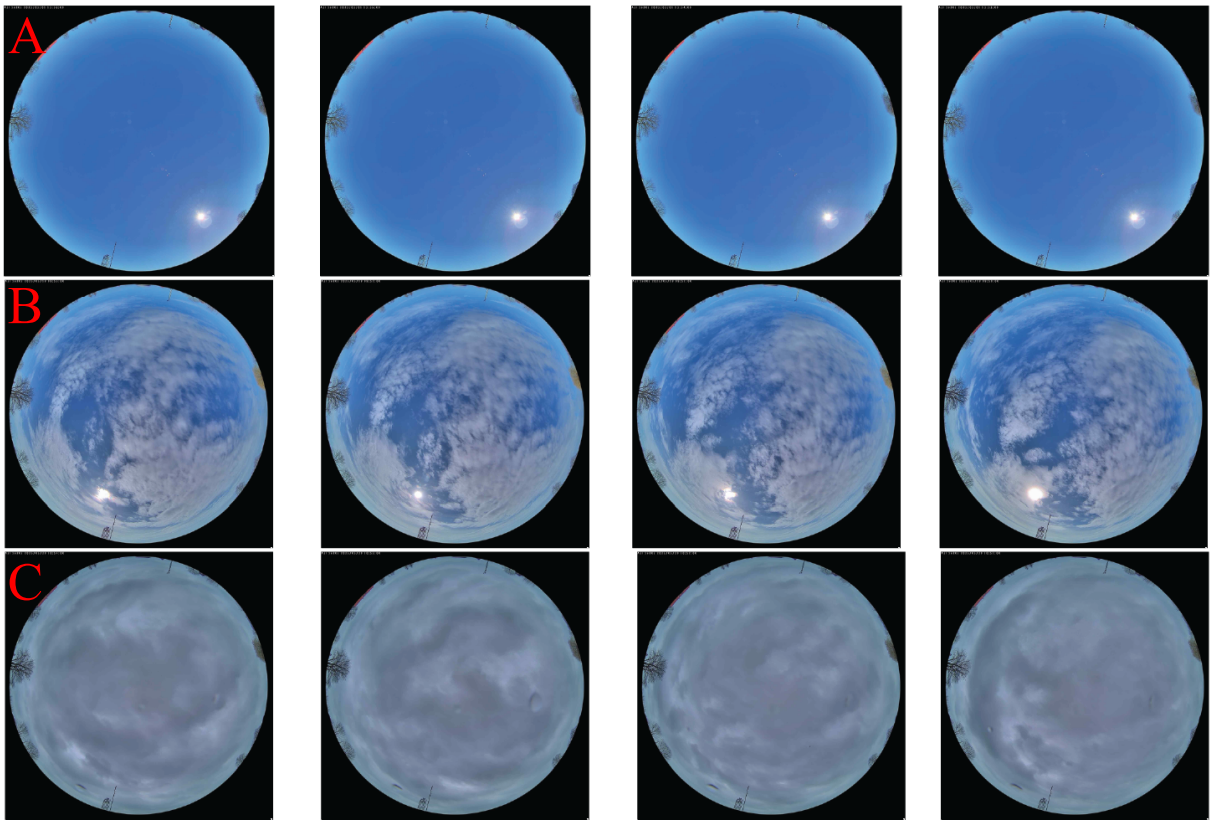

Figure 7. Sequence of sky images by ASI-16 in different weather conditions (acquired at KNMI site Cabauw). (A) Four sequential sky images on a clear day captured from 13:36:00, March 1st, 2023. (B) Four sequential images of an overcast day captured from 09:53:00, Mach, 18th. (C) Four sequential images of a fully cloudy day captured from 10:54:00, March 20th.

The four sky images of Figure 7A, starting capture at 13:36:00 on March 1, 2023, exhibits a sequence of sky images on a clear sky-day. Figure 7B, starting capture at 09:53:00 on March 18, depicts a partly overcast sky (>70% clouds) where a thick layer of clouds forms a uniform, gray expanse, effectively obscuring the sky and sunlight in some parts. The moving clouds close to the sun will lead to fast irradiance changes when the clouds pass the sun. Finally, Figure 7C, starting capture at 10:54:00 on March 20, presents a fully cloudy day with substantial cloud cover, however less dense than that in Figure 7B. The cloud distribution in this image permits occasional views of the blue sky, offering insights into the diversity of cloud formations.

In summary, the SolFasi project has successfully established a robust network of All-Sky cameras, adeptly overcoming initial installation challenges and Covid restrictions through collaboration and expertise. The planning and execution of the camera installations, data

networking, and storage systems signify an important milestone in the project and allows for the development of PV power generation forecasting. The imagery captured across various weather conditions, as showcased in the figures, underscores the potential of this technology to provide valuable insights into dynamic cloud formations and their direct influence on solar irradiance.

3.2. Methodology

In this research, our primary objective is to harness the potential of an all-sky imaging network, comprising sophisticated cloud cameras, to analyze movement of clouds and predict their future course up to one hour ahead. This prediction is crucial for accurately forecasting solar photovoltaic (PV) power generation on the ground. From the four all-sky imagers a large database has been generated including images, meteorological parameters from KNMI, and solar irradiance. Our approach encompasses the development of innovative algorithms for creating 3D cloud information and 2D cloud shadow fields using advanced machine learning techniques. Despite facing challenges in networking and data integration, particularly in correlating shadow fields with PV power, we have made significant steps in analyzing cloud dynamics and their impact on solar energy forecasting.

The scope of the developed methodology can be subdivided in three parts:

I. **Cloud Detection Methodology:** This part details the methodology for detecting and analyzing clouds from sky images, including the algorithms used and the results obtained from these methods. This includes the pre-processing and analysis of all-sky image data to accurately identify cloud patterns and characteristics.

II. **Analysis of Cloud Motion and 2D Shadow Mapping:** Here, the process of using selected features from the cloud detection phase to analyze cloud motion is described, how cloud base height can be obtained, and how to create a 2D shadow map on the ground. This part of the methodology elaborates on how these features are instrumental in understanding cloud dynamics and their subsequent impact on solar irradiance.

III. **Innovative Method for Cloud Base Height Determination:** The third step of our methodology introduces an innovative approach for determining cloud base height using a network of *N* cameras. This technique will utilize the collective data from multiple

imaging points to enhance the accuracy and reliability of cloud base height measurements, contributing significantly to our understanding of cloud behavior and movement.

This methodology forms the backbone of our research, aiming to significantly enhance the precision of solar PV system performance predictions.

3.2.1. Cloud Detection Methodology

Cloud detection plays a critical role in short-term solar forecasting, which is key to predicting the impact of cloud cover on solar radiation [12]. This section delves into various techniques for short-term forecasting, emphasizing the use of sky imagers for accurate cloud detection. Essential to this process is the effective pre-processing of sky images and the deployment of automatic cloud detection methods for precise pattern identification. Among these, so-called superpixel techniques have emerged as particularly effective in enhancing cloud detection capabilities.

The advancement in automated cloud detection marks a significant shift from traditional manual labeling methods. Automated techniques, leveraging sophisticated computer vision and machine learning algorithms, offer a more efficient and accurate approach to identifying cloud patterns [13-15]. The pre-processing of sky images is a crucial step in this context. It involves refining the images to accentuate relevant features for cloud identification, thereby preparing the data for a more impactful analysis.

Superpixel segmentation stands out in this realm, offering a refined approach to grouping pixels based on their similarities. This technique generates superpixels that create more coherent and interpretable segments of the image, crucial for detailed cloud pattern analysis [16,17]. The Simple Linear Iterative Clustering (SLIC) algorithm exemplifies this approach. SLIC forms compact and uniform superpixels that adhere to cloud boundaries in an image, enhancing the precision of cloud pattern identification [18].

The integration of advanced pre-processing steps with state-of-the-art automatic cloud detection methods, particularly superpixel segmentation, significantly improves the accuracy and efficiency of cloud detection. This advancement is pivotal for enhancing the overall reliability of short-term solar forecasting.

Data Collection

We deploy the cloud detection method on data collected from two CMS-Schreder ASI-16/50 cameras installed at the Cabauw BSRN site [19], located in the west of the Netherlands (51.971100° N, 4.926700° E and 51.970000° N, 4.926389° E) and managed by KNMI, as we initially had limitations in accessing data at the UU locations. The installation of these cameras is depicted in Figure 8. The distance between the cameras is 759.56 meters.

Each camera is equipped with a robust coated quartz glass dome, 180°/360° fish-eye optics, and a 4-Megapixel resolution sensor (1920×1920 pixels Fish eye), and includes an IR-cut filter to prevent sensor degradation from long-term direct sunlight exposure. The ASI-16/50 camera contains built-in ventilation and up to 60W airflow heating, which helps to minimize

Figure 8. Skycam locations at the Cabauw BSRN station, The Netherlands.

condensation on the glass dome and quickly removes raindrops and snow, ensuring clear imaging. This system has been tested to operate effectively in harsh environments, withstanding temperatures ranging from -40°C to over +50°C. Its double-cover design and

forced ventilation are specifically tailored to reduce damage risks due to prolonged exposure to intense direct sunlight. Additionally, the cameras come with temperature and humidity sensors.

Proposed methodology

The methodology for this study centers around data collected from all-sky imagers located in Cabauw, The Netherlands. Specifically, we have selected days featuring a variety of weather conditions—clear skies, partial cloudiness, and overcast—to ensure a comprehensive analysis across a spectrum of cloud covers. This is depicted in the dataset, which consists approximately 400 sky images, each paired with its manually labeled counterpart to serve as a ground truth for validation, as shown in Figure 9.

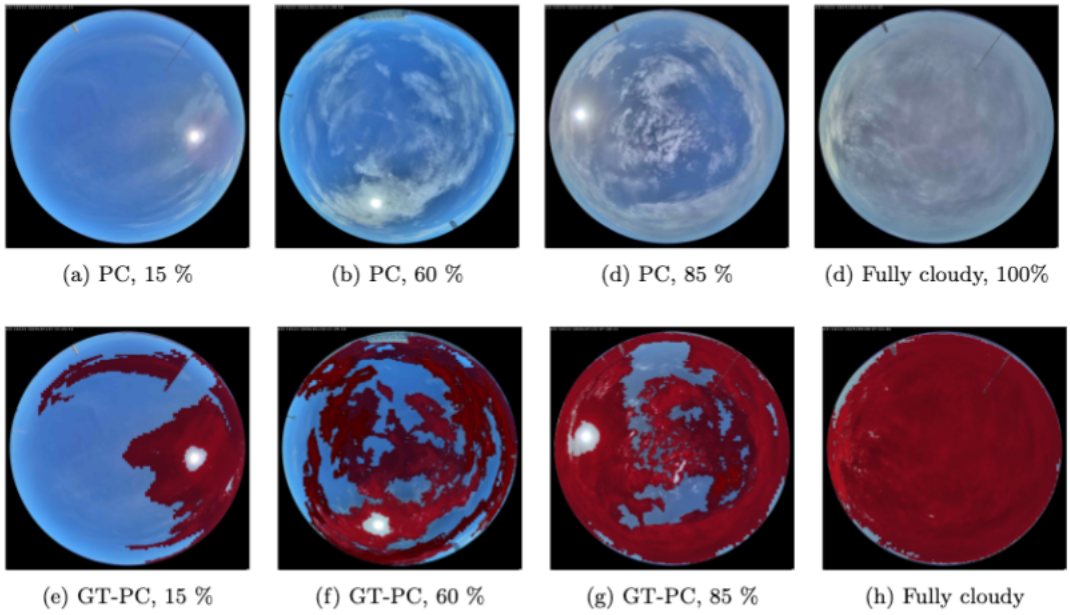

Figure 9. Acquired sky images (a)-(d) and their corresponding ground-truth (GT) (e)-(h) manually segmented. Images are aquired at KNMI site Cabauw [19]. Four images with different cloud cover percentages are analysed, ranging from partially cloudy (PC, 15%-60%-85%) to a fully cloudy sky.

To improve the quality of the sky images, we have implemented a series of pre-processing steps. Initially, images are converted from JPG to PNG format to benefit from the latter's lossless nature. Subsequent steps involve applying a Gaussian blur with a 7x7 pixel kernel to smooth out irregularities, followed by a Laplacian operator of the same kernel size to accentuate edges. Additionally, we evaluate the standard deviation of luminance across a 7x7 pixel area to gauge the average pixel variation within its vicinity. Further enhancements include

image resizing (de-fisheye), noise reduction, image distortion correction, and contrast adjustment—all aimed at optimizing the images for subsequent analysis. Resultls of these pre-processing efforts are illustrated in Figure 10.

Following pre-processing, we apply superpixel segmentation techniques, namely SLIC [18], Watershed [20], and Felzenszwalb algorithms [21], to group pixels into meaningful regions based on similarity. This effectively segments the cloud regions from the clear sky areas, as explained in the flowchart provided in Figure 11.

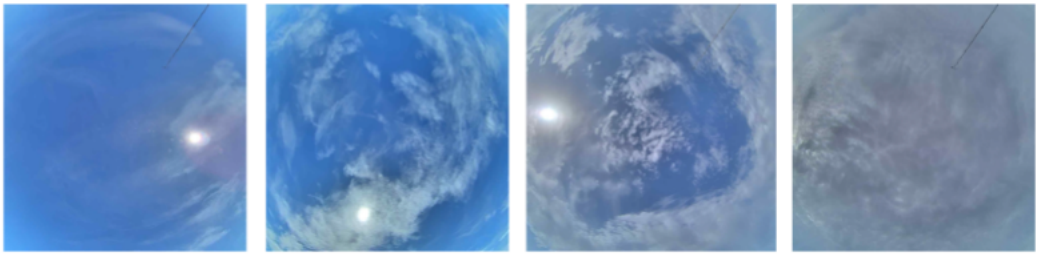

Figure 10. Example of a sky images pre-processed using a linear De-fisheye (library in Python). Images correspond to images (a)-(d) in Figure 9.

Validation of the segmentation accuracy involves extracting key cloud features, such as shape, texture, color, and spatial information, from the segmented regions. These features are then juxtaposed with those from the ground truth images to assess congruency. The performance of the segmentation techniques is quantified using the metrics precision, recall, and F1 score (see details below).

Proposed superpixel technique for automatic cloud labeling

In this study, a novel algorithm for automatic cloud labeling and detection based on the superpixel-based Technique (SPT) is proposed. The algorithm consists of two steps: firstly,

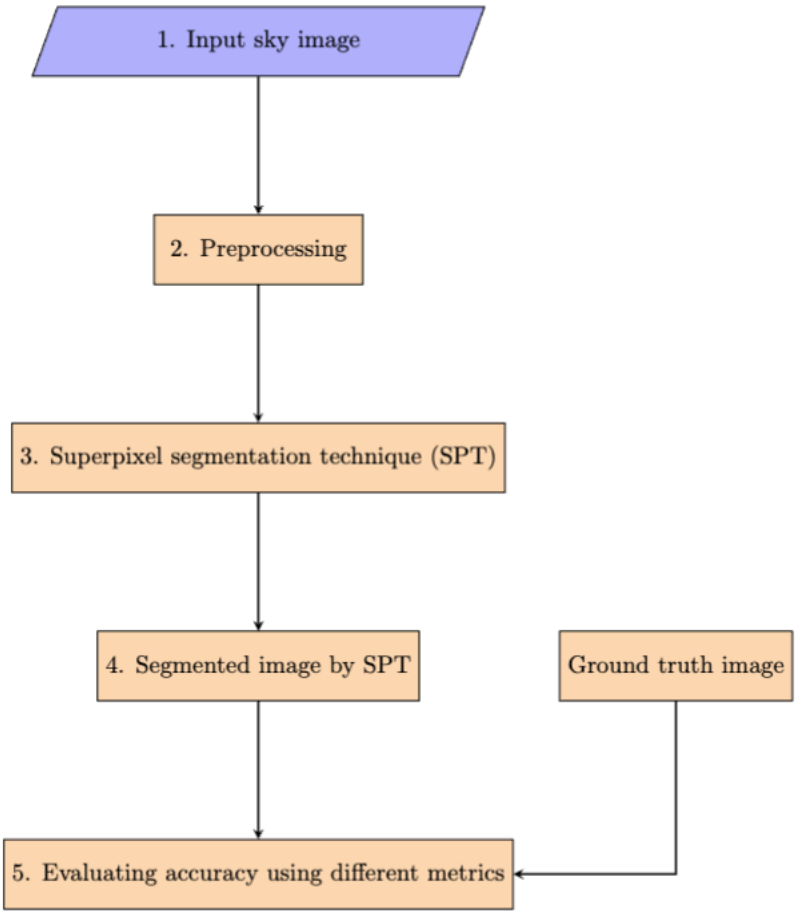

Figure 11. Flowchart for Sky Image Segmentation.

applying a selected SPT to cluster pixels in ground-based cloud images using contour and texture characteristics to ensure consistent grouping within each superpixel, and secondly, validating the accuracy of the technique in automatically detecting clouds using these superpixels.

In this subsection, three SPT algorithms were studied: 1) Superpixel Linear Iterative clustering SLIC [18], 2) Watershed [20], and 3) the Felzenszwalb algorithm [21]. The SLIC algorithm is a popular superpixel-based approach for cloud detection in sky images. It aims to divide an image into compact and meaningful regions (superpixels) based on color and spatial proximity. The algorithm follows a step-by-step process to achieve accurate and efficient cloud segmentation, the flowchart is depicted in Figure 12.

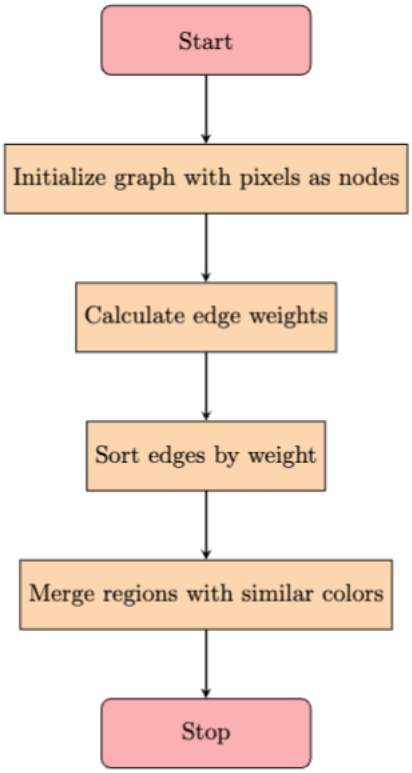

Figure 12. Flowchart of the SLIC algorithm.

The 5-dimensional distance D is defined as:

$$D = \sqrt{D_{color}^2 + (\frac{M}{S} \times D_{space})^2}$$

$$S = \sqrt{\frac{K}{N}}$$

where *K* is the desired number of superpixels and *N* is the total pixels of the image and *M* is the compactness factor. D_{color} is the color distance between a pixel and its assigned superpixel center, and D_{space} is the spatial distance between the pixel and the center.

The color distance D_{color} is calculated using the Euclidean distance between the pixel color (*R*, *G*, *B*) and the superpixel center color (R_c, G_c, B_c):

$$D_{color} = \sqrt{((R - R_c)^2 + (G - G_c)^2 + (B - B_c)^2)}$$

The spatial distance D_{space} is calculated using the Euclidean distance between the pixel coordinates (x, y) and the superpixel center coordinates (x_c, y_c):

$$D_{space} = \sqrt{((x - x_c)^2 + (y - y_c)^2)}$$

A compactness term M is also incorporated in the objective function to ensure superpixel compactness.

Comparison and Evaluation metrics

In comparison to state-of-the-art methods, in this study, the Red-Blue Ratio (RBR) method is considered to be a technique to compare the superpixel techniques with, due to its higher accuracy [22]. It relies on analyzing the ratio between the red and blue color channels in digital images. This method leverages the fundamental optical properties of the Earth's atmosphere to distinguish between clear sky and cloudy conditions [23]. In this technique, it is well-established that clear sky conditions scatter blue light more effectively than they do red light, thus affecting their intensities in the images. On the other hand, clouds scatter both blue and red light roughly equally. As a result, the RBR method calculates the ratio of red (denoted as Ir) to blue channel (denoted as Ib) intensities in the images. This ratio is used as a key indicator for cloud detection. The RBR is expressed mathematically as:

$$RBR = \frac{Ir}{Ib}$$

However, the RBR is not uniform across the entire sky hemisphere in clear conditions. Several factors contribute to this non-uniformity. One significant factor is the presence of aerosols in the atmosphere and the effects of air mass (AM). Due to the size distribution of aerosols relative to the wavelength of visible light, the scattering of light by aerosols exhibits a weaker wavelength dependence than scattering by gas molecules. Consequently, this leads to scattered light appearing whiter, which translates to a reduction in the saturation of the blue color channel [24]. This phenomenon becomes particularly evident near the horizon, where the relative optical air mass increases and more aerosols are present along the optical path through the atmosphere. Additionally, in the circumsolar region (around the sun), forward scattering effects of aerosols contribute to a whiter appearance.

The Boundary Recall metric quantifies the superpixel segmentation algorithm's ability to accurately capture the boundaries between different regions in an image. The Boundary Recall is defined as the number of correctly detected boundaries (*True Positives$_{bnd}$*) over the sum of correctly detected boundaries and missed boundaries (*False Negatives$_{bnd}$*).

$$Boundary\ Recall\ = \frac{(True\ Positives_{bnd})}{(True\ Positives_{bnd} + \ False\ Negatives_{bnd})}$$

Recall, also known as True Positive Rate or Sensitivity, measures the proportion of true positive superpixels (*True Positives$_{sp}$*) correctly identified by the segmentation algorithm. It represents the algorithm's ability to capture all the relevant superpixels in the image.

$$Recall\ = \frac{\left(\ True\ Positives_{sp}\right)}{\left(True\ Positives_{sp} + \ False\ Negatives_{sp}\right)}$$

Precision quantifies the algorithm's accuracy in correctly assigning labels to the superpixels.

$$Precision\ =\ True\frac{Positives_{sp}}{\left(True\ Positives_{sp} + \ False\ Positives_{sp}\right)}$$

The F1-Score is a harmonic mean of Precision and Recall, providing a balanced measure of the algorithm's accuracy.

$$F1 - Score\ =\ 2\ \times \frac{(Precision\ \times\ Recall)}{(Precision\ +\ Recall)}$$

The F1-Score ranges from 0 to 1, with a higher value indicating better segmentation accuracy. In order to determine true and false positives and negatives, a ground truth must be available for every image analyzed. We have analyzed all images manually, identifying clouds, clear sky, and the Sun. The images analyzed comprise a wide variety of weather conditions.

Results

This section presents the findings obtained from employing various superpixel techniques with different parameter configurations across diverse weather conditions. The analysis of the results encompasses evaluation metrics such as precision, recall, and F1-score values. Through a comprehensive examination of the outcomes, numerous patterns and observations emerge, providing valuable insights into the performance of these techniques as an automatic manual labeling technique.

While we have analyzed a large dataset for the purpose of clarity, we selected four different cloud covers to compare the effectiveness of the three superpixel segmentation algorithms, i.e., 15%, 60%, 80%, and 100% (overcast). These are depicted in the corresponding Figure 13.
The segmentation was carried out across various settings, allowing us to investigate the impact of varying parameters, including the number of segments (100, 200, 250) and compactness (10, 20, 30). Features were subsequently extracted from these superpixels, encompassing essential

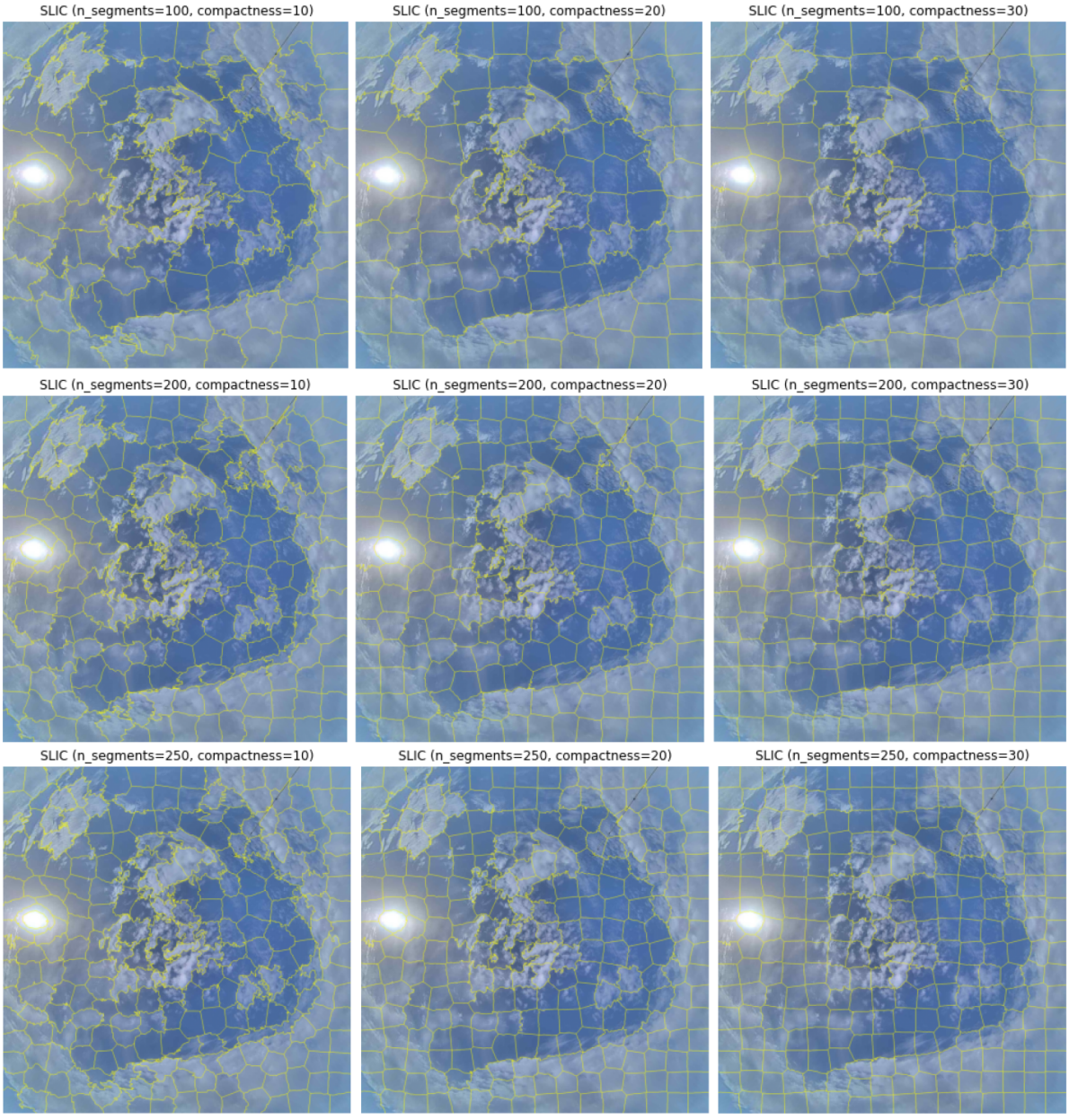

Figure 13. Illustration of SLIC superpixel segmentation results with various segment numbers and compactness levels.

attributes such as mean color, mean intensity, and region size. Notably, we also calculated the Red/Blue (R/B) ratio as an additional feature. The image was then thresholded using Otsu's method to derive an automatic threshold value, as illustrated in Figure 14.

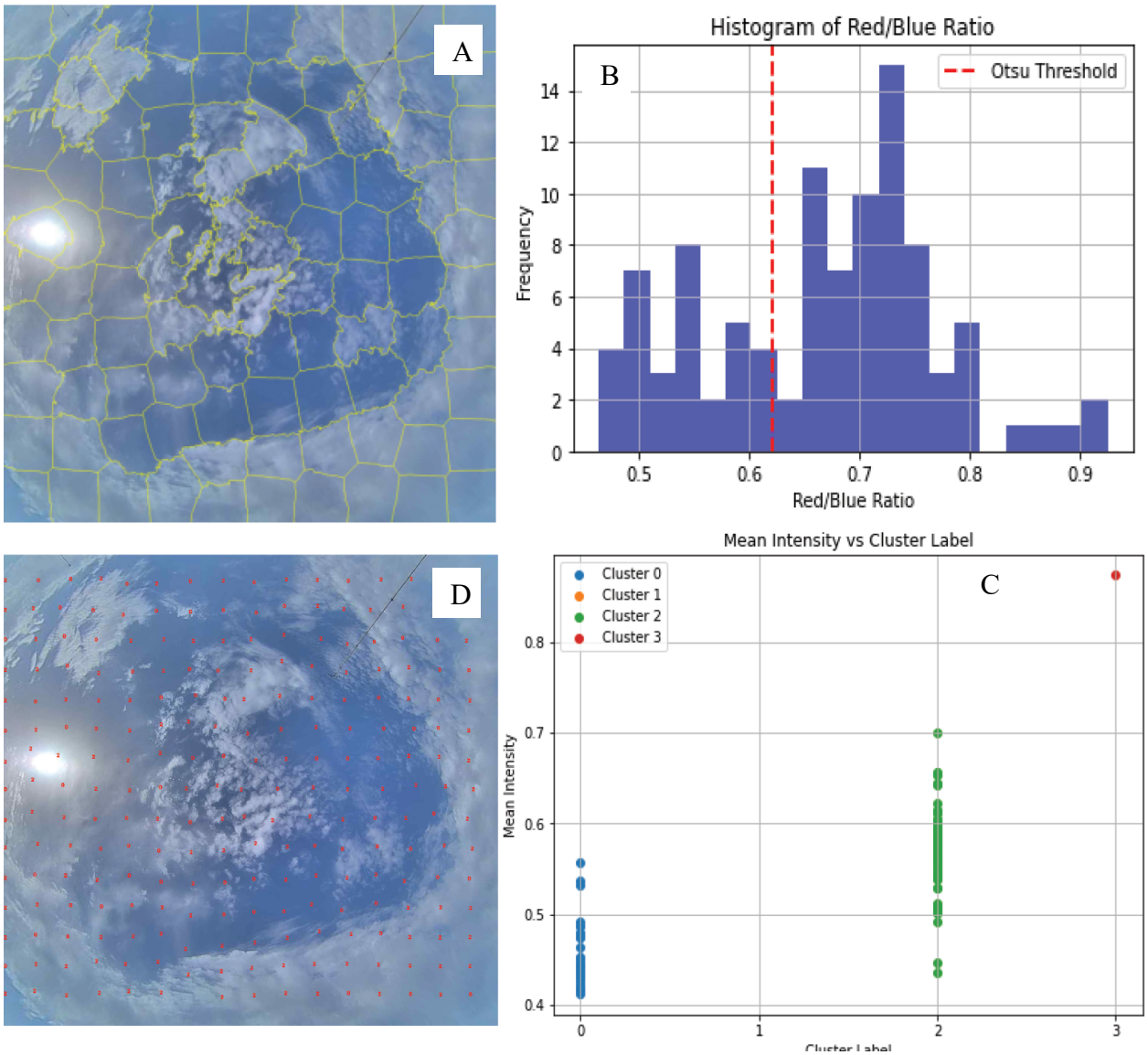

Figure 14. Comprehensive cloud recognition process: (A) original segmented image, (B) red-blue ratio histogram representation, (C) scatter plot of Intensity vs. Cluster Label - Higher intensity corresponds to Cluster Label 3, representing the sun, and (D) final cloud detection process, with cluster numbers added in the image.

Table 1 summarizes the performance of the SLIC algorithm under different cloud cover conditions, showing precision, recall, F1-score, and accuracy percentages. Table 2 details the performance for the other methods.

Table 1. Evaluation Metrics for the Segmentation Based SLIC Algorithm for Different Weather Conditions.

Cloud cover (%)	Precision (%)	Recall (%)	F1-Score (%)	Accuracy (%)
15	81.47	80.78	81.09	80.78
60	84.52	80.85	72.29	80.85
85	66.13	64.31	64.94	64.31
100	71.58	71.37	71.29	71.37

Table 2. Evaluation Metrics for the Segmentation Based RBR, Watershed and Felzenswalb Algorithms for Different Weather Conditions.

RBR				
Cloud cover (%)	Precision (%)	Recall (%)	F1-Score (%)	Accuracy (%)
15	27.27	27.27	27.27	27.38
60	33.55	33.55	33.55	34.21
85	29.67	29.67	29.67	19.70
100	97.41	97.41	97.41	97.42
Watershed				
Cloud cover (%)	Precision (%)	Recall (%)	F1-Score (%)	Accuracy (%)
15	66.43	66.43	66.43	64.31
60	35.21	35.21	35.21	41.96
85	47.54	47.54	47.54	45.49
100	42.84	42.84	42.84	38.04
Felzenswalb				
Cloud cover (%)	Precision (%)	Recall (%)	F1-Score (%)	Accuracy (%)
15	77.8	77.2	77.4	77.2
60	56.0	58.7	56.1	58.7
85	80.1	77.1	78.1	77.1
100	49.6	46.1	46.7	46.1

The SLIC algorithm demonstrated consistent performance across various weather scenarios. It achieved impressive accuracy and remarkably high precision, leading to a very high F1-Score, and showcased its proficiency in delineating cloud boundaries, as evident from its boundary recall. Also, both the Watershed and Felzenswalb superpixel segmentation performed well in clear sky and overcast weather conditions but encountered challenges in fully cloudy scenarios. The RBR method displayed varying performance across different weather scenarios. While it excels with remarkable accuracy (97.42%) and high precision (97.41%) in overcast conditions with 100% cloud coverage, it faced substantial challenges in clear sky and partly cloudy scenarios.

To summarize, superpixel-based SLIC segmentation demonstrated remarkable consistency and adaptability across various weather scenarios, making it the most suitable choice for cloud detection in the context of short-term solar forecasting. This comparative analysis not only highlights the effectiveness of these segmentation techniques but also underscores the importance of selecting the most appropriate method based on the specific weather conditions encountered. This contributes to more accurate short-term solar forecasting and enhances the efficient utilization of solar energy, thereby addressing the crucial need for reliable cloud detection in the context of optimizing solar energy integration into the power grid.

3.2.2. Analysis of Cloud Motion and 2D Shadow Mapping

This second part of our research is dedicated to enhancing the accuracy of Photovoltaic (PV) output forecasting, deploying two of more sky cameras and a machine learning algorithm combined with physical modeling. Our goal is to improve the forecasting of solar irradiance on an intra-hour scale. This part Is guided by two research questions:

1. What is the efficacy of determining ground-level 2D shadow fields using a network of sky cameras?
2. How does the accuracy of this 2D projection method compare against other existing techniques?

In this study, we aim to provide a comprehensive overview of the methodologies and key findings from our research.

At the core of our approach is an algorithm designed to process images for identifying cloud blocks, determining cloud base height, tracking cloud motion, determination of 2D cloud shadow fields and evaluating transmittance. These processes converge to create a Global Horizontal Irradiance (GHI) map over an area of 10x10 km^2, capable of forecasting up to 30 minutes in advance. Results were validated using GHI data from CAMS (Copernicus Atmosphere Monitoring Service) [25] and compared with a smart persistence approach.

Methodology

The methodology outlined in this research is shown in Figure 15. First, data is collected from sky cameras located in Almería, Spain, due to a temporary limitation in accessing the camera data from the Netherlands. This was part of a collaborative effort within IEA PVPS Task 16. Location details were 37.091549° N, -2.363556° E for camera #1 (ASI1) and 37.095253° N, -2.354785° E for camera #2 (ASI2), at a distance of 880.2 m. To assess the algorithm's robustness, the chosen data will come from a day exhibiting a mix of sky conditions. This imaging data is augmented with irradiance data from CAMS, which is accessed via PVlib functions [26]. The CAMS data offers irradiance values with a temporal resolution of one minute based on Numerical Weather Prediction models.

Based on earlier work on sky-images based forecasting [27-30], the Support Vector Machine (SVM) method was selected [31]. With this method, the connected component and manual division algorithms delineate and segregate cloud blocks, which are crucial for analyzing cloud base height and motion. The precise identification of cloud blocks is further refined by implementing viewing angle limitations and a solar mask, allowing for more accurate cloud base height and movement analysis. This pre-processing and feature extraction allow for the next steps: cross-correlation for cloud motion assessment and, ultimately, the determination of irradiance maps and forecasts.

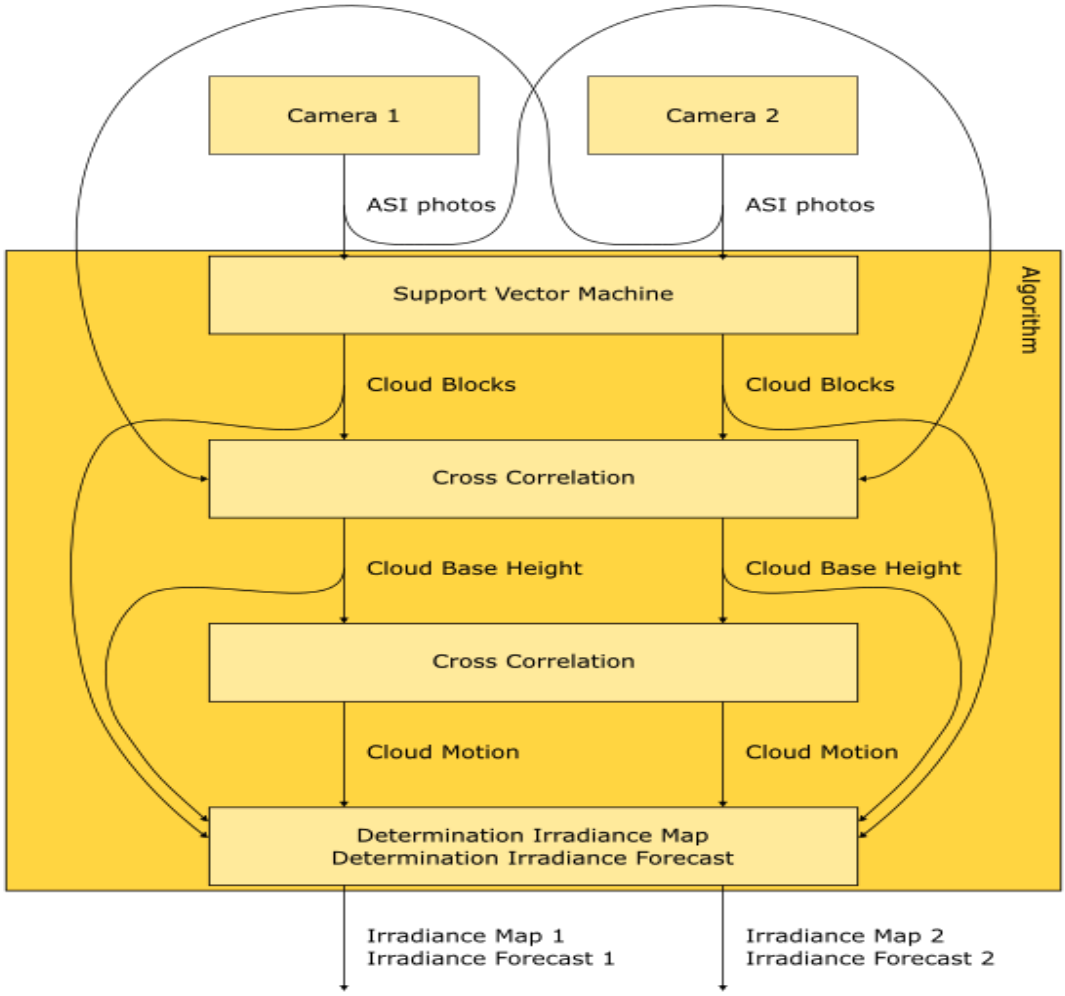

Figure 15. An overview of the methods and algorithm that are applied.

Image pre-processing and cloud block detection:

The process of identifying cloud pixels can begin once irrelevant pixels have been masked. The distinction between cloud and clear sky is based on the scattering properties of light in the atmosphere. The RGB values captured in the images from the cameras are key to differentiating these two. With developed methodologies, thresholds applied to these color channels enable the discernment between cloudy and clear sky pixels where the R/B ratio can be particularly indicative.

The All-Sky Imagers lack spectral and neutral density filters and respond variably to different lighting conditions. This response is contingent upon the camera model, necessitating manual and often complex calibration for each setup. To address this, adaptive thresholding through

supervised machine learning techniques has been employed, where classifiers such as k-nearest-neighbors, binary decision trees, and neural networks have been utilized for cloud classification [32-35].

The binary classification method by Peng et al. [32] has been adapted for this algorithm, which distinguishes pixels using six features based on the R/B ratio. The first four features are derived directly from the pixel values themselves: Red Value, Blue Value, Green Value, and R/B Ratio. The remaining two features consider the neighboring pixels: the fifth feature uses the Laplacian of the Gaussian across a 7x7 pixel area, useful for edge detection, and the sixth calculates the standard deviation of the luminance in a similar area, representing the pixel's average contrast with its surroundings.

The classifier in use, a Support Vector Machine (SVM), treats each pixel as a multi-dimensional vector, where each dimension corresponds to a pixel feature. The SVM constructs a hyperplane that maximizes the margin between two classes of pixels—cloud or sky—thereby minimizing the influence of outliers. This optimization also accounts for errors and uncertainties inherent in the manually labeled training data [32].

Training of the SVM requires pixels from training photos to be labeled as cloud or sky, forming a binary image. These binary images, alongside the original photos, calibrate the SVM through supervised learning. An example of such a training photo and its corresponding labeled binary image is demonstrated in Figure 16A and 16B. Upon successful identification of cloud pixels, the cloud masks are transformed into cloud blocks, following the approach by [32]. This conversion is illustrated in Figure 16C, where individual cloud entities within the mask are given bounding boxes. Smaller cloud objects are filtered out to avoid unnecessary noise and to focus on larger blocks significant for analysis. These larger blocks are then subdivided into smaller sections, facilitating more precise tracking of their movement and position. The resulting cloud blocks are the foundation for the subsequent analysis stages.

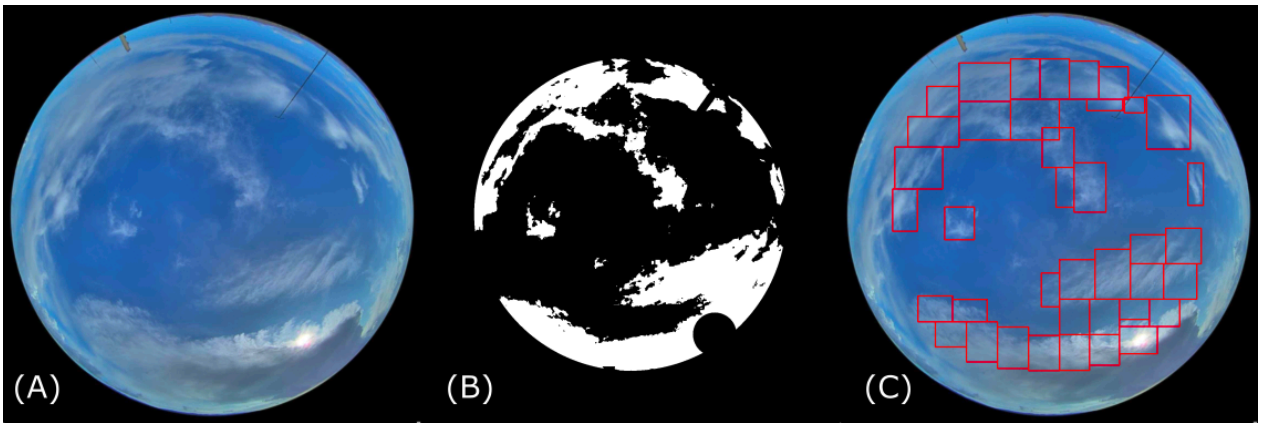

Figure 16. (A) image to be analysed by SVM, (B) cloud mask as identified by the SVM, (C) corresponding cloud blocks that were determined.

The second step involves confining viewing angle to reduce errors at low viewing angles that could otherwise distort cloud positioning and appearance. Objects within the camera's field of view, particularly the sun, are then identified and masked to prevent misclassification during the cloud detection process, see Figure 17.

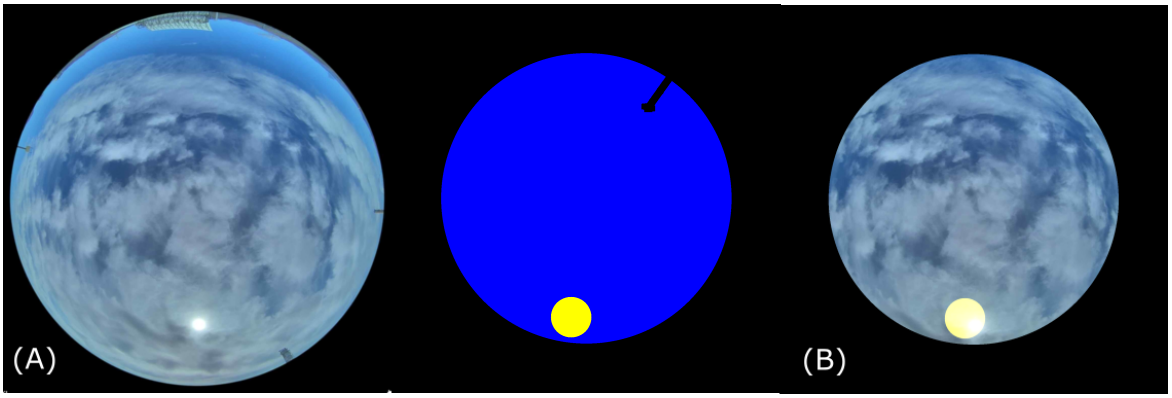

Figure 17. (A) original image, (B) sun mask in yellow that is used to mark the area close to the sun, and combined image. Image is aquired at KNMI site Cabauw.

In the third step of the cloud analysis methodology, the primary objectives are to ascertain the Cloud Base Height (CBH) and Cloud Motion of cloud blocks. This is achieved by linking cloud blocks across different images, a task accomplished through the application of Zero Mean Normalized Cross Correlation (ZMNCC). ZMNCC is a template-matching technique that scans a cloud block across another photo to identify the best matching area, effectively tracking the

cloud from one image to the next. In this technique, cloud blocks are interlinked using the method by Peng et al. [32]. ZMNCC can be mathematically expressed as:

$$R = \frac{1}{n}\sum_{x,y}\frac{1}{\sigma_f \sigma_t}\left(f(x,y) - \mu_f\right)\left(t(x,y) - \mu_t\right)$$

where $f(x,y)$ denotes the image to be scanned for template t, μ_f and σ_f are the mean and standard deviation of $f(x,y)$, μ_t and σ_t are the mean and standard deviation of $t(x,y)$, and n is the number of template pixels $t(x,y)$. The template images, or cloud blocks, are used to scan the image. The maximal value of R indicates the optimal match location between the template and the scanned image. This method is vital for understanding cloud dynamics and contributes significantly to the accuracy of the solar forecasting algorithm.

By employing two cameras and utilizing ZMNCC, the CBH of the cloud blocks is computed through triangulation methods. This triangulation is visualized in Figures 18 and 19. The geometry involved in this method is crucial; it relies on the azimuth and altitude angles of a cloud block as observed from the locations of the two cameras. Initially, the azimuth angles (θ_1, θ_2) captured by both cameras are used to calculate the angles α, β, and γ within the triangle formed between the two cameras and the cloud block.

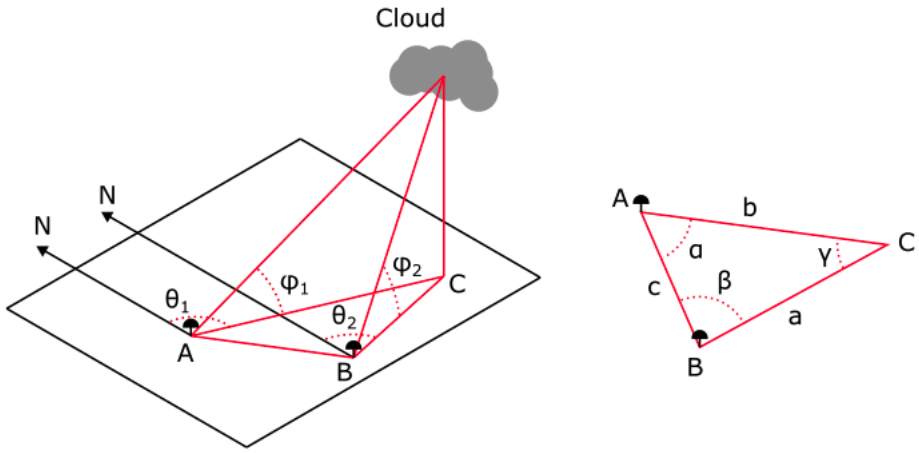

Figure 18. The geometry used for determining the CBH. Camera #1 is located at position A, and camera #2 is located at position B.

Once the cloud blocks have been interlinked between photos from the dual-camera setup, triangulation techniques are employed to calculate the CBH. This involves using the known distance between the cameras as a base and applying the observed angles to triangulate the position of the cloud. As there are two cameras, we can determine CBH using camera #1 as main camera or #2. Following the CBH calculation, cloud motion is determined by analyzing two consecutive photos from the same camera, which reveals the cloud's displacement over time, as seen in Figure 19. This process not only measures the distance clouds travel but also provides insight into the speed and direction of cloud movement, which are vital parameters for forecasting solar irradiance.

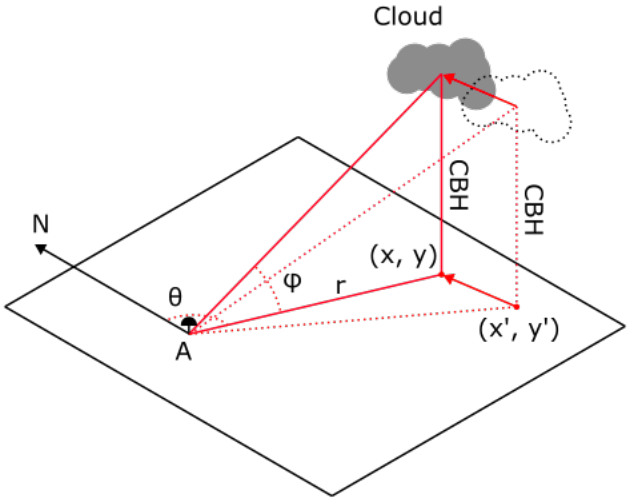

Figure 19. An illustration of the underlying geometry that is exploited to determine the cloud motion. (x, y) is the current ground position of the cloud, and (x', y') is the past ground position of the cloud.

Determining and Forecasting the Irradiance Map:

Following the calculation of cloud base height, the next critical task is to construct an irradiance map, a two-step process that starts with creating a binary shadow map to pinpoint cloud shadow locations. This step is grounded in the geometry illustrated in Figure 20, which guides the determination of the cloud's ground position (shadow). With the cloud's position and CBH known, the next phase involves calculating the ground distance to its shadow, using the sun's elevation angle, and then pinpointing the shadow's location relative to the cloud based on the sun's azimuth angle. The SVM-generated cloud mask is instrumental in shaping the shadow on

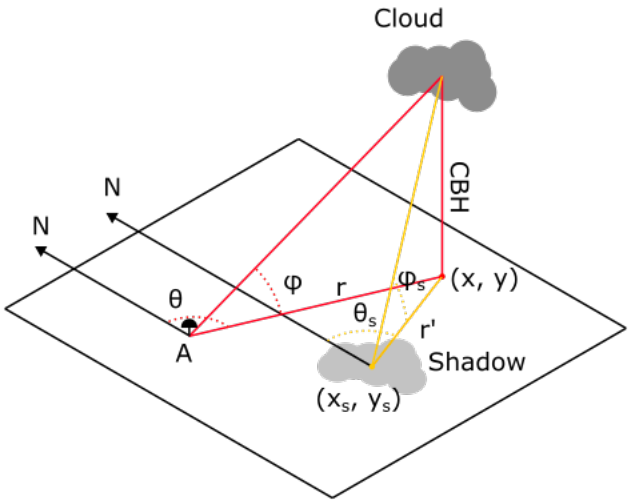

Figure 20.The geometry that is used for determining the locations of cloud shadows on the ground.

the map, with each cloud pixel being evaluated for its shadow counterpart, ensuring consistency in CBH across all pixels within a cloud block.

The construction of the binary shadow map paves the way to the second step: calculating the map's irradiance levels, i.e., a map of GHI. The Clear Sky Model provides the baseline for these calculations [12, 36]. The actual irradiance is determined by modifying the clear sky irradiance based on cloud transmittance, where the luminance of cloud blocks informs the degree of transmittance, following a simple linear relationship with the maximum luminance set at a value of 255. With the cloud positions and motions known, short-term forecasts of cloud and sun positions are generated, allowing for the prediction of irradiance maps for intervals ranging from 1 to 30 minutes. The generation of irradiance maps for varied time intervals necessitates a thorough analysis of cloud movements and positions over time. By tracking these changes, the model is capable of predicting future cloud locations for upcoming intervals. This predictive information, coupled with the baseline data from the Clear Sky Model, allows for the nuanced adjustment of irradiance levels to reflect the anticipated cloud cover at each specific interval. Consequently, a dynamic irradiance map is produced, offering a time-sensitive reflection of the solar energy availability.

Validation:

The forecast is validated against irradiance data from the CAMS database. Root Mean Square Error (RMSE) and the Mean Square Error (MSE) are used to assess accuracy. The results are also compared against a smart persistence approach, which is a simple and naïve approach, not relying on ASI images. The forecasting algorithm is compared against the smart persistence by determining the forecast skill (FS). The following equations define RMSE, MSE and FS:

$$RMSE = \sqrt{\frac{1}{n}\sum_{i=1}^{n}(Forecast - Measurement)^2}$$

$$MSE = \frac{1}{n}\sum_{i=1}^{n}(Forecast - Measurement)^2$$

$$FS = 1 - \frac{RMSE_{Algorithm}}{RMSE_{Persistence}}$$

Results:

First, SVM results are evaluated for its efficacy in cloud pixel identification. Second, the outcomes related to the Cloud Base Height and Cloud Motion determination are detailed. And third, the results obtained from the irradiance map and its subsequent forecasts are investigated.

Cloud Identification using SVM

The performance of the SVM in identifying cloud pixels is illustrated in Table 3. The accuracy of true cloud detection, while significantly lower than the benchmark set by [32] is counterbalanced by a higher success rate in true sky detection. This discrepancy is attributed to the limited dataset used, comprising only 22 fully cloudy images captured on a day characterized by predominantly overcast skies. The confusion matrix presented in Table 3 lays out these details, demonstrating the SVM's strengths and weaknesses in distinguishing between cloud and sky pixels.

Table 3. Performance of the SVM for Cloud Pixel Identification

	Manual Detection Cloud	Manual Detection Sky
SVM Cloud	71.9%	28.1%
SVM Sky	7.1%	92.9%

Further scrutiny of the SVM's performance highlights a particular challenge faced during times of sunrise and sunset. These periods appear to affect the SVM's accuracy, likely due to the unique lighting conditions present at these times. An illustrative example is given in Figure 21, showcasing photos taken shortly after sunrise and just before sunset, alongside the corresponding cloud masks generated by the SVM. Table 4 shows the SVM's performance during these transitional light conditions, with sunrise and sunset data revealing a marked decline in cloud detection efficacy, underscoring the need for algorithmic adjustments to handle the varying lighting conditions encountered throughout the day.

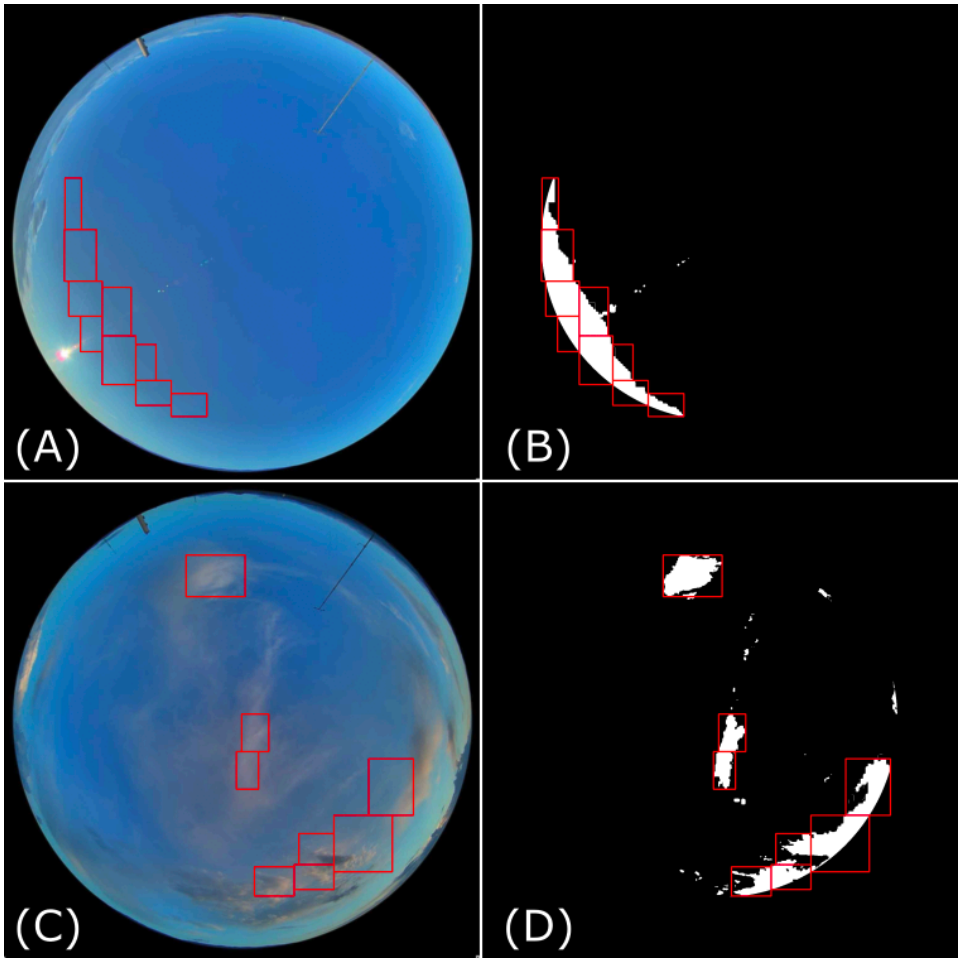

Figure 21. (A) image taken right before sunset, (B) corresponding cloud mask created by the SVM, (C) image taken right after sunset, (D) corresponding cloud mask. Images are aquired at KNMI site Cabauw.

Table 4. SVM Performance at Sunrise and Sunset

	Manual Detection Cloud	Manual Detection Sky
Sunrise cloud detection		
SVM Cloud	19.1%	81.9%
SVM Sky	1.6%	98.4%
Sunset cloud detection		
SVM Cloud	17.1%	82.9%
SVM Sky	2.2%	97.8%

Cloud base height

The analyzed images show distributions of CBHs, see Figure 22. Differences are seen from either using camera #1 or #2 as main camera. Overal, CBH values range from 0 to 12,500 meters, which can be expected. Average CBH is about 2000m. Camera #1 readings align with this expected range 97.4% of the time, indicating a high degree of reliability in its measurements. On the other hand, Camera #2 demonstrates a lower congruence, with only 70.5% of its readings falling within the anticipated range. Inspection of the image data from Camera #2 revealed partial data corruption, which likely influenced its performance. This issue was only identified towards the end of the research, precluding the possibility of re-evaluating the dataset.

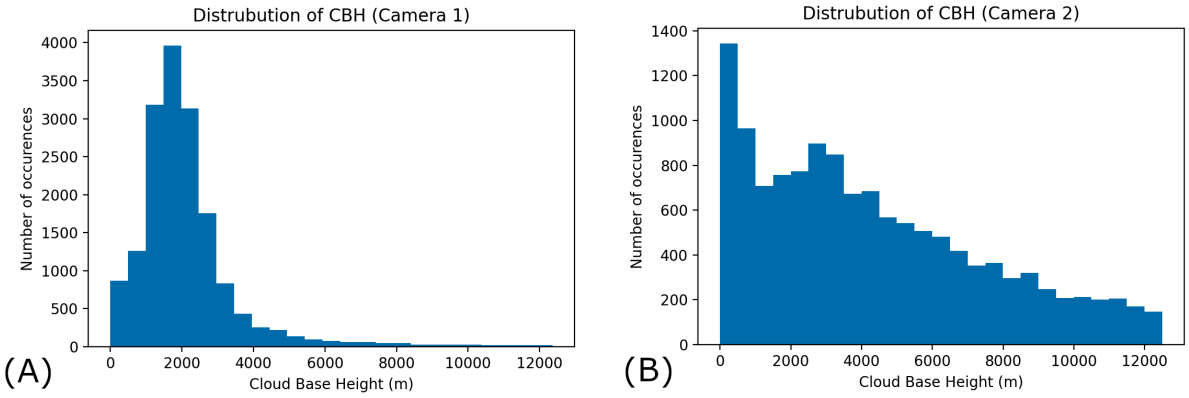

Figure 22. Distribution of CBH determined from camera #1 and #2. (A) shows CBH using camera #1 as the main camera, and (B) shows CBH using camera #2 as the main one.

Cloud Motion:

The cloud motion analysis, a crucial aspect of understanding atmospheric dynamics, shows notable differences between the data captured by two cameras. Literature benchmarks the expected cloud motion (speed) to range between 0 and 35 m/s. From the measurements obtained, Camera #1 demonstrated a high degree of accuracy, with 91.2% of its readings falling within this expected range. However, for camera #2, only 67.2% of its readings within the anticipated motion parameters.

Scatter plots and histograms for both cameras offer a visual representation of these findings as represented in Figure 23. The dataset, encompassing data from a single day, showed a consistent direction in cloud movement. This uniformity is particularly evident in the histogram from Camera #1, which displays a pronounced peak at 3-5 m/s, corroborating the theory that clouds in a given area are likely to move in a similar direction due to uniform wind conditions.

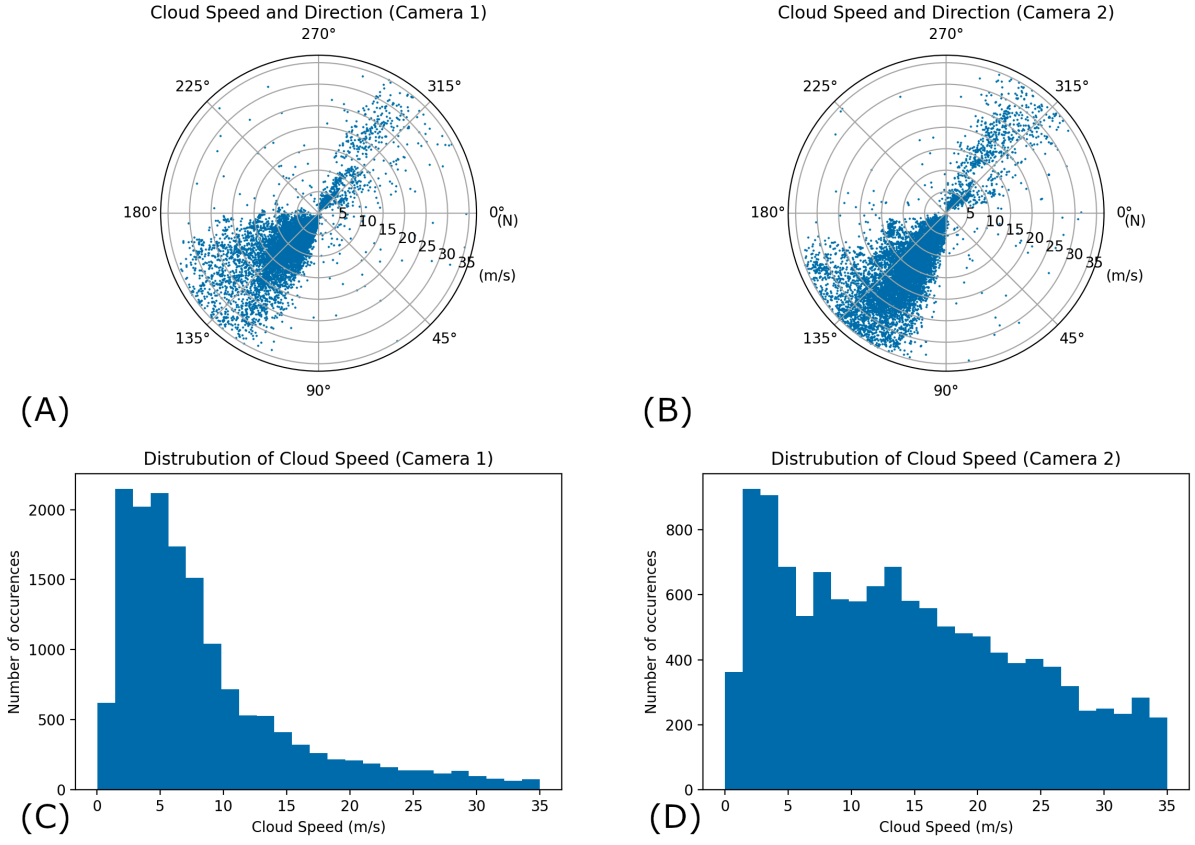

Figure 23. Scatter plots of the estimated cloud motion for camera #1(A) and camera#2 (B). North is 0 degrees. Histograms for the speed of the clouds for camera #1(C) and camera#2 (B).

This is further reflected in the fact that individual cloud blocks, often part of the same larger cloud formation, exhibited similar speeds.

The results from Camera #2, while capturing the same peak in cloud speed, presented a more even distribution across different speeds, diverging from the focused peak observed in Camera #1's data. Given the dataset's temporal limitation to one day, a narrower distribution would typically be more indicative of actual conditions, as clouds subjected to the same wind patterns tend to move at similar speeds. The broader distribution from Camera #2 suggests anomalies, which could be attributed to corrupted images.

The directionality of cloud motion was consistent across both cameras, showing two notable peaks in the histograms, one primary and one secondary, directly opposite the first. This phenomenon might be explained by the mathematics involved in the algorithm, where trigonometric functions prone to discontinuities require adjustments, sometimes involving the addition or subtraction of π to maintain accuracy in the computations.

While Camera #1 provided results that closely matched expected cloud speeds and directions, the performance of Camera #2 was hindered by data quality issues, impacting its reliability. The consistent direction of cloud movement and the primary speed peak support the validity of the cloud motion measurements from Camera #1, reinforcing its data's usefulness in contributing to accurate atmospheric analysis and forecasting.

Irradiance map and forecast:

The performance of the irradiance forecast algorithm across varying forecast horizons is analyzed, with the algorithm displaying commendable accuracy in comparison to literature benchmarks. It is found that the errors decrease with longer forecast times, which contrasts with literature that typically anticipates increased error over longer periods. This anomaly is likely due to the limitations of the CAMS data, which may lack the necessary spatial and temporal resolution to validate the method effectively.

The algorithm's irradiance predictions (shadow maps) are mapped across a 10x10 km^2 area, with a resolution of roughly 10x10 meters, as shown in the example of the irradiance map in Figure 24. The irradiance forecasts, plotted alongside CAMS-determined irradiance, reveal fewer

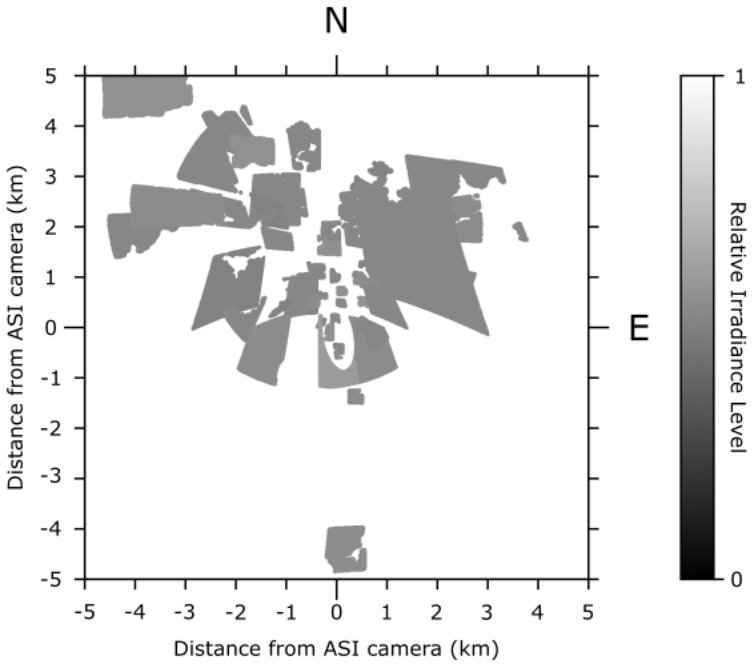

Figure 24. A relative irradiance map, as generated by the algorithm. A value of zero reflects zero irradiance, a value of 1 reflects maximum irradiance, which is equal to the clear sky GHI of that moment, as determined by the clear sky model.

and shorter periods of shading than expected, which becomes increasingly evident with forecasts beyond 15 minutes. At these longer intervals, the clouds initially detected move beyond the frame of view, and upcoming clouds that could create shadows are not yet visible, resulting in almost no shading periods observed.

The accuracy of the irradiance predictions is quantified through MSE, RMSE, and FS. Camera #1 shows 0-minute RMSE of 50.66 W/m^2, and Camera #2 showing an RMSE of 80.32 W/m^2. The results, summarized in a Table 5, 6 and 7, reveal that the algorithm maintains or improves performance at extended forecast horizons compared to persistence, which defies the typical expectation of diminishing accuracy. Figure 25 details GHI based on CAMS data, as well as forecasts for lead times of 0 – 30 minutes.

Table 5. The Mean Squared Error ((W/m^2)^2) and Root Mean Squared Error (W/m^2) (also expressed in percentage of the highest measured value) of the irradiance map predictions at the location of the camera, when determined by the algorithm.

Algorithm	Camera #1		Camera #2	
Forecast horizon	MSE	RMSE	MSE	RMSE
0 min	2566.7	50.7 (8.3%)	6451	80.3 (13.2%)
1 min	2166.3	46.5 (7.6%)	4424.9	66.5 (10.9%)
5 min	1618.0	40.2 (6.6%)	5126.0	71.6 (11.8%)
15 min	1518.6	39.0 (6.4%)	1519.1	39.0 (6.4%)
30 min	1518.6	39.0 (6.4%)	1804.9	42.5 (7.0%)

Table 6. MSE ((W/m^2)^2) and RMSE (W/m^2) (also expressed in percentage of the highest measured value) of the irradiance map predictions at the location of the camera, when determined by smart persistence.

Smart persistence	Camera #1		Camera #2	
Forecast horizon	MSE	RMSE	MSE	RMSE
1 min	17.0	4.1 (0.7%)	17.0	4.1 (0.7%)
5 min	358.3	18.9 (3.1%)	358.4	18.9 (3.1%)
15 min	1881.8	43.3 (7.1%)	1882.4	43.4 (7.1%)
30 min	2285.1	47.8 (7.8%)	2285.8	47.8 (7.8%)

Table 7. FS of the irradiance map predictions at the location of the camera.

	Camera #1	Camera #2
Forecast horizon	FS	FS
1 min	-11.4	-18.6
5 min	-1.46	-2.5
15 min	0.07	-0.65
30 min	0.18	0.18

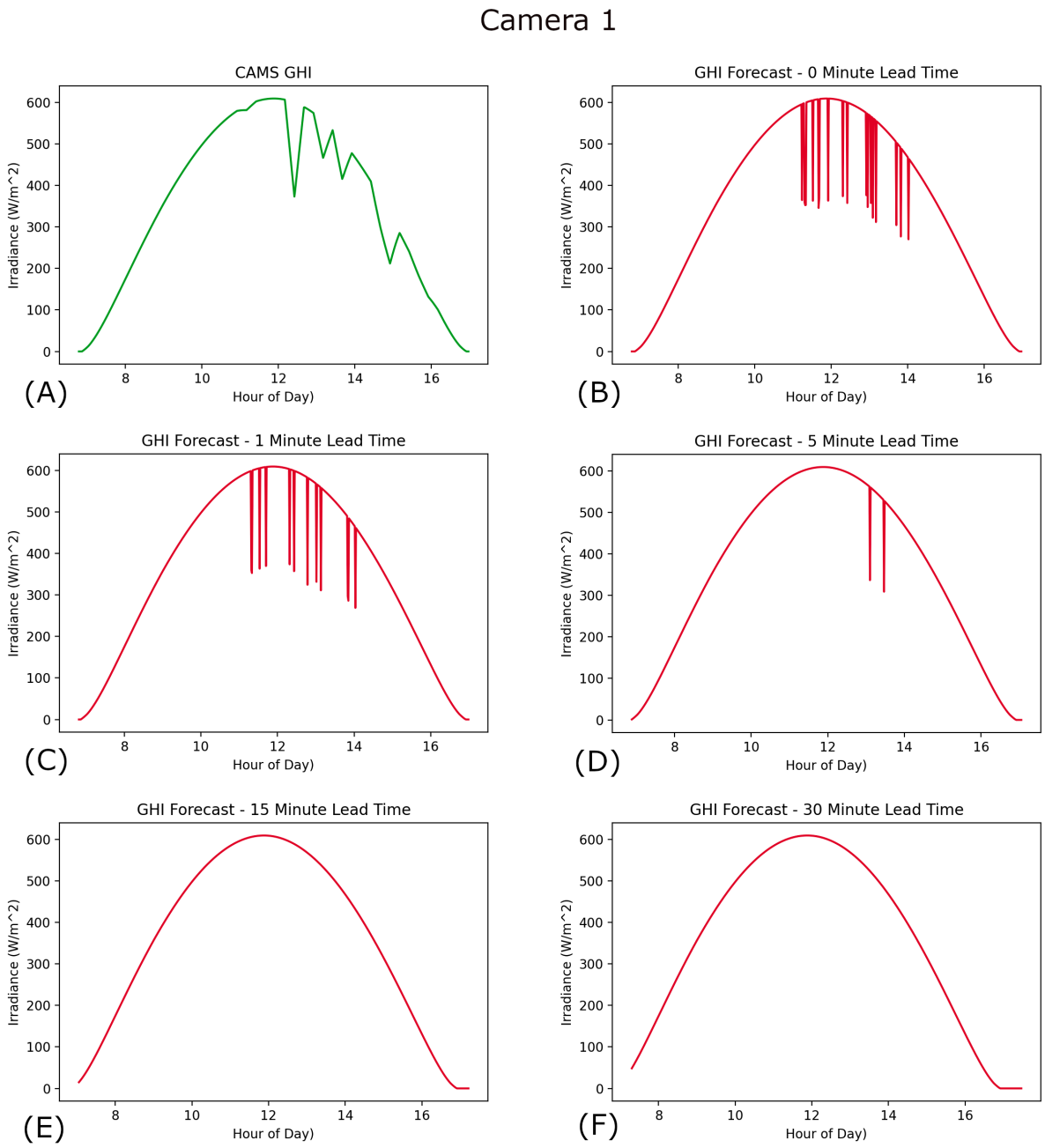

Figure 25. (A) GHI as determined by CAMS for camera 1. (B)shows the GHI as determined by the algorithm, for 0 min lead time. (C), (D), (E), and (F) show the GHI forecasts with lead times of 1, 5, 15, and 30 minutes, respectively.

In conclusion, this research aimed to advance the forecasting of solar irradiance on an intra-hour timescale using two All Sky Imagers (ASIs). The study hinged on the development and implementation of a machine learning algorithm for processing imagery, identifying cloud blocks, and subsequently determining cloud base height, cloud motion, and transmittance to

create an accurate irradiance map spanning 10x10 kilometers and providing forecasts up to 30 minutes.

The algorithm's performance, assessed over a day with variable sky conditions, initially appears consistent with other established methods documented in literature. Also, our targets of a relative root-mean-square-error (rRMSE < 10%) is met (see Table 6), while that of the forecast skill (FS>20%) is nearly met (see Table 7). It was observed that, while the smart persistence approach surpasses the algorithm in the very short-term forecasts (less than 10 minutes), the machine learning approach demonstrates improved accuracy for longer timescales. This suggests the potential of machine learning algorithms in enhancing the utility of ASIs for solar irradiance mapping.

A critical observation from the research is that the limited dataset and possible shortcomings in data quality are principal factors contributing to lower accuracy levels in the algorithm's performance. Addressing these limitations could significantly refine the forecasting capabilities of the model.

As a future direction, networking multiple ASIs to enrich the dataset and applying the refined algorithm promises to yield a more robust application. This progression is expected to contribute substantively to the operational implementation of photovoltaic (PV) power systems, optimizing their performance in accordance with real-time solar irradiance variations influenced by cloud movements.

3.2.3. Innovative Method for Cloud Base Height Determination

At the core of short-term solar forecasting is the accurate estimation of CBH using sky imagers, a critical parameter in determining the speed and subsequent positions of cloud shadows on the ground [37,38]. While various methods to estimate CBH exist, ranging from satellite to ceilometric measurements, each comes with its limitations [39-42]. A recent approach circumvents the computational intensity of traditional methods by narrowing the search area in image analysis [43].

This section explores how epipolar geometry can be used to optimize CBH estimation. The theoretical foundation and the operational potential of this approach may lead to an important improvement in our ability to forecast solar irradiance.

Proposed method

The heuristic method, essential for CBH identification in sky imaging, is an advanced approach combining image processing and geometrical analysis.

Epipolar geometry states that in the case of two cameras whose locations and angles are known with regards to an object, taking a photograph of that bject sufficient information is available to exactly determine the position of the object in (real-world) 3D space. Additionally, if the object's position on the first image is known, its possible location on the second image is restricted to a line on that image, known as the *epipolar line* [44]. This relationship can be formalized using the *fundamental matrix F* [45]:

$$p_2^T F p_1 = 0$$

Here, p_1 and p_2 are the locations of the same real-world object on camera 1 and 2, respectively. In particular, this implies that Fp_1 defines the epipolar line of point p_1 in image 2, as this line will contain those coordinate vectors p_2 in image 2 that satisfy the above equation. Notably, the fundamental matrix is constant for a pair of two cameras (provided that they are not moved or turned with respect to each other) and hence it can be pre-computed. In the context of sky imaging for CBH determination, this implies that the computational effort of matching cloud sections on two images can be considerably reduced (searching *along a line* rather than in an entire image) at almost no cost, as the fundamental matrix is pre-computed. In addition, software packages such as *OpenCV* that implement efficient algorithms to determine *F* based on an image pair from two cameras are readily available [46].

Once a cloud block in the image of camera 1 has been identified, its epipolar line in the image of camera 2 can be calculated with low effort. However, once this happened, the exact cloud block needs to be found in camera 2's image. To this end, in the approach used by Nguyen and Kleissl [43] correlation coefficients *ρ* of the cloud block in image 1 and all cloud blocks located on the epipolar line of camera 2 are computed. The correlation coefficient *ρ* is based on the correlation of the saturation levels of the pixels located at the same position of image 1 and image 2. The cloud block that maximizes *ρ* is then identified as the right one.

To reduce the computational effort even further, it is possible to devise heuristic schemes that have the goal to decrease the number of correlation coefficients *ρ* that need to be calculated even beyond what is achieved through computing the epipolar line. Here, the feasibility of one such heuristic scheme has been investigated. Its core assumption is that in most cases, the CBH of one cloud block will not be extremely different to those next to it. Thus, this scheme does not foresee the calculation of *all* correlation coefficients across the epipolar line, but only of those related to cloud blocks that would correspond to a CBH *close to the one* that was obtained for the previously computed cloud block (assuming that this cloud block was adjacent to the current one). If adjacent cloud blocks indeed to have similar CBHs (particularly if they belong to the same cloud), then this scheme is expected to lead to another substantial reduction in computational effort, particularly for in the context of an eight-camera setup. The detailed workflow for the first cloud block - which shows most fundamental concepts of the heuristic method - is shown in Figure 26, and the scheme for cloud blocks 2 and beyond is shown in Figure 27.

Key steps in implementing this method include:

1. Computation of the Fundamental Matrix: Utilizing OpenCV's `findFundamentalMat` function, the fundamental matrix *F* is estimated from two images of the same scene taken by different cameras. This matrix is crucial for correlating points between the two images.
   The fundamental matrix was computed and was found to be:

$$F = \begin{bmatrix} 2.99\ 10^{-6} & 5.90\ 10^{-5} & -1.67\ 10^{-2} \\ 5.21\ 10^{-5} & -6.94\ 10^{-6} & 5.37\ 10^{-2} \\ 1.57\ 10^{-2} & -4.71\ 10^{-2} & 1 \end{bmatrix}$$

2. Epipolar Line Calculation: The computation involves multiplying *F* with the coordinates of the cloud block's center pixel in the first image. This step is fundamental in narrowing down the search area in the second image.

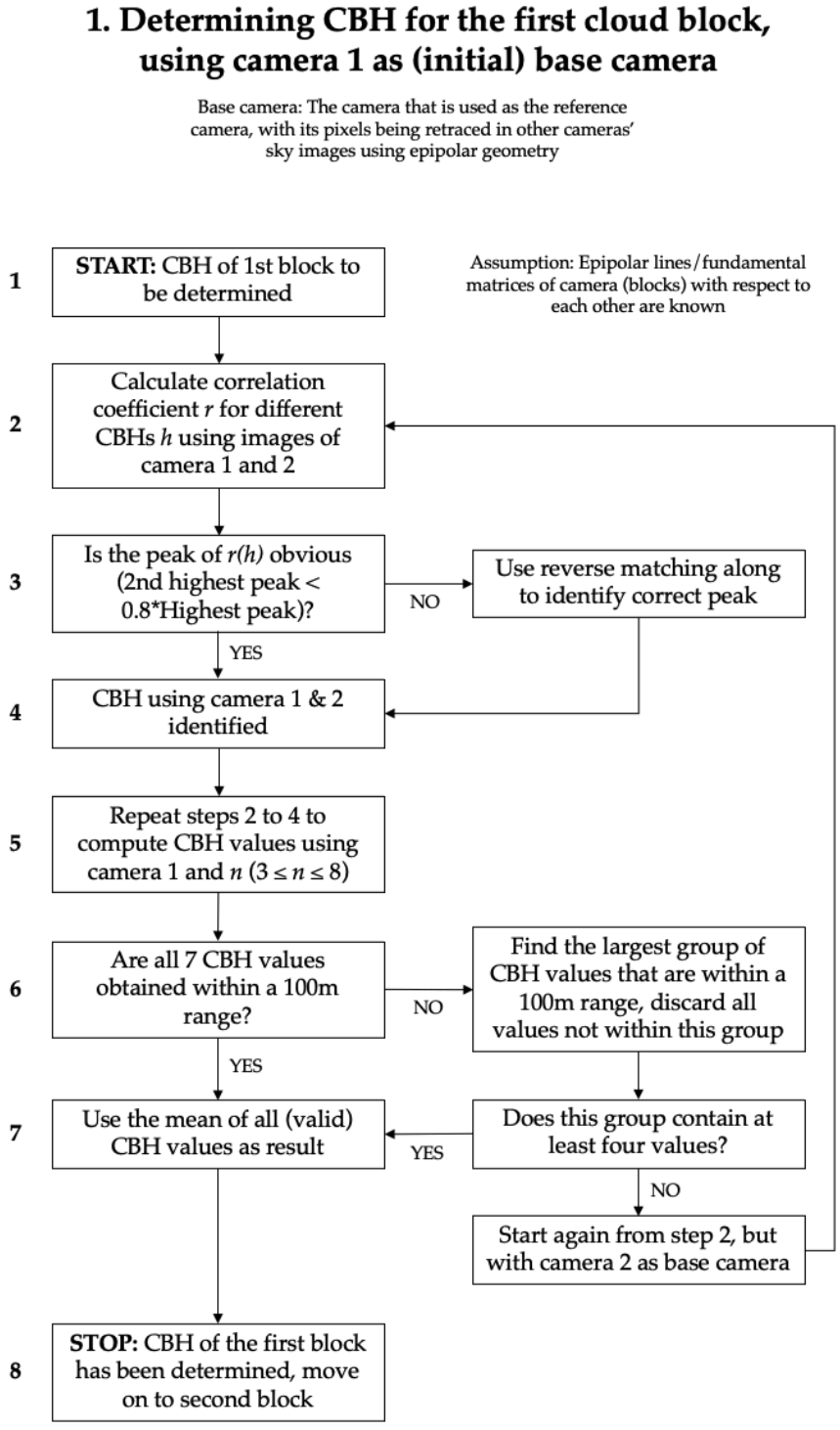

Figure 26. CBH determination workflow for the first cloud block.

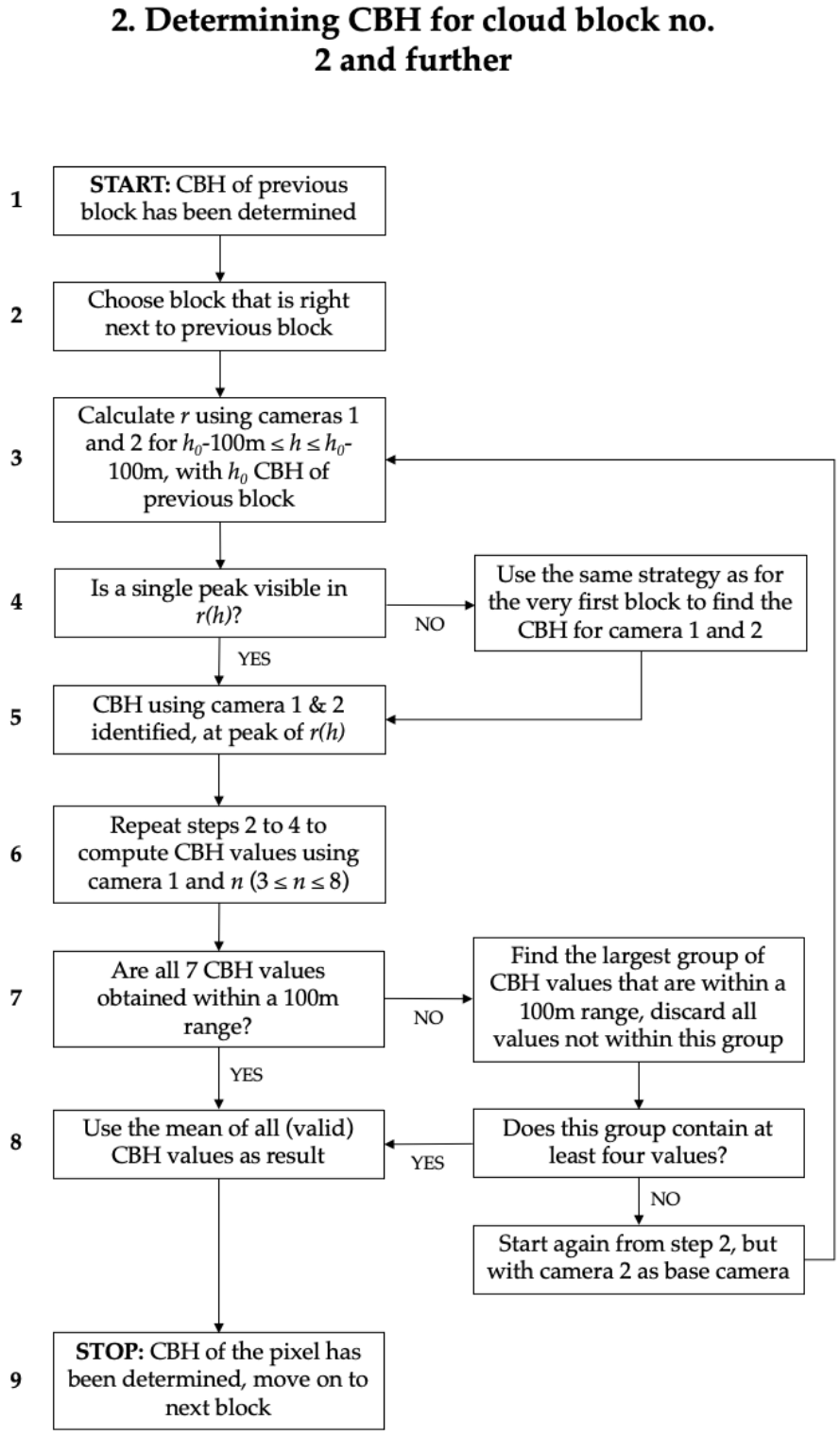

Figure 27. CBH determination workflow for the for the second and later cloud blocks.

3. Identifying Corresponding Points for Prior CBH: By calculating the intersection of the epipolar line with a circle representing the prior CBH radius, the matching point in the second image is identified. This step uses optimization techniques to ensure accuracy.
4. Cropping of the Second Image: To enhance efficiency, the second image is cropped around the identified point, creating a smaller search area for template matching.
5. Acceptance Criteria for Heuristic Results: The algorithm employs correlation thresholds and feasibility checks for CBH to determine the validity of results. This includes discarding implausible CBH values and relying on full template matching if needed.
6. Computational Effort Evaluation: While not directly impacting the method's execution, understanding the computational savings offered by the heuristic approach is crucial. This is assessed by comparing execution times.

In the optimization and evaluation phase, the method's performance is gauged based on accuracy and computational efficiency. The main parameters—correlation threshold and cropping dimensions—are experimentally optimized to balance accuracy with reduced computational demands.

In section 3.2.2, CBH was determined based on image pairs from two imagers. As no ceilometers or similar pieces of equipment were used for a non-stereographic measurement of CBH, the values obtained there are used here as the a-priori true values. This method has been reported to producing accurate results [43]. It is expected that implementing the heuristic method leads to a (very) moderate reduction in CBH estimation accuracy while allowing for a significant reduction of computational power needed. Based on the exact results, contexts in which applications of the heuristic method are appropriate can be identified.

Results

The heuristic method was executed under variation of two different process parameters: The number of pixels added to the cloud block at all sides (step 4), and the threshold value that the maximum correlation point needs to reach in order to accept the template match (step 5).

Values between 25 and 300 pixels were tried for the former variable, and values between 0.50 and 0.95 for the latter variable. Results are shown in Table 8.

Table 8. Most important result characteristics when applying the heuristic method for CBH determination. Column *Heur. Scheme*: share of cloud blocks for which the heuristic scheme was used, column *CBH feasible*: fraction of times the resulting final CBH was reasonable (above 700 m and below 8500 m), Column *Non-heur. Check*: share of cloud blocks for which the result of the heuristic method showed the same result as a non-heuristic calculation, Column *Rel. time saving*: total relative time saved when using the heuristic rather than the full method for all images.

Add. pixels	Threshold	Heur. scheme	CBH feasible	Non-heur. check	Rel. time saving
25	0.50	0.09	0.64	0.92	0.04
25	0.60	0.07	0.65	0.94	0.02
25	0.70	0.04	0.66	0.97	-0.00
25	0.80	0.03	0.67	0.98	-0.02
25	0.90	0.01	0.68	1.00	-0.03
25	0.95	0.00	0.68	1.00	-0.04
50	0.50	0.24	0.60	0.84	0.19
50	0.60	0.21	0.62	0.87	0.16
50	0.70	0.17	0.64	0.91	0.11
50	0.80	0.11	0.66	0.97	0.07
50	0.90	0.08	0.68	0.99	0.03
50	0.95	0.04	0.68	1.00	-0.01
100	0.50	0.51	0.51	0.77	0.45
100	0.60	0.45	0.56	0.83	0.38
100	0.70	0.41	0.59	0.87	0.34
100	0.80	0.35	0.63	0.92	0.29
100	0.90	0.21	0.68	0.99	0.15
100	0.95	0.10	0.68	1.00	0.04
150	0.50	0.63	0.53	0.76	0.54
150	0.60	0.59	0.55	0.79	0.50
150	0.70	0.52	0.60	0.86	0.43
150	0.80	0.44	0.65	0.93	0.35
150	0.90	0.27	0.68	0.98	0.19
150	0.95	0.12	0.68	1.00	0.03
200	0.50	0.65	0.58	0.81	0.54
200	0.60	0.62	0.60	0.84	0.50
200	0.70	0.54	0.64	0.92	0.43
200	0.80	0.49	0.68	0.96	0.36
200	0.90	0.32	0.68	0.99	0.22
200	0.95	0.13	0.68	1.00	0.03
300	0.50	0.43	0.66	0.90	0.28
300	0.60	0.41	0.67	0.92	0.26
300	0.70	0.39	0.67	0.94	0.24
300	0.80	0.34	0.69	0.98	0.19
300	0.90	0.24	0.68	0.99	0.09
300	0.95	0.09	0.68	1.00	-0.05

The following observations can be made:

- The area added to the cloud block in image 2 should not be too small. Otherwise, the prior CBH needs to be extremely close to the actual CBH for the actual matching point to be included in the cropped version of image 2. When adding only 25 pixels, the heuristic scheme almost never yields a result and the CBH needs to be computed using the non-cropped image 2 after all. For this reason, adding very few pixels in combination with a low threshold value can even increase the overall computational workload of the algorithm as first, the heuristic scheme is applied but then in almost all cases the full calculation still needs to be made.
- Using a too low correlation threshold results in false-positive CBH estimations. The column *Non-heur. check* in Table 8 shows the share of cloud blocks for which the result yielded by the heuristic method was the same as when using a non-cropped image 2 for template matching all the time. This effect is most extreme when using medium-sized crops for image 2: When adding 100 or 150 pixels to the cloud block, about 1 in 4 cases yield a false-positive result with a correlation threshold of 0.5. These false-positives do yield a drastic reduction of computation time (around 50 %), but at a high accuracy cost. When increasing the number of pixels added, the false positives decrease likely due to the probability of the actual matching point being in the cropped image increasing.
- Conversely, choosing a too high correlation threshold is also ineffective as this leads to false-negatives in the heuristic scheme leading to unnecessary computational effort of performing template matching on the entire image 2 while the match could have been made on the cropped image had the threshold been lower.
- In general, while the accuracy of the heuristic scheme increases with increasing pixels added to the cloud block in image 2, it decreases again when adding very large pixel buffers: for all correlation thresholds, the heuristic scheme results in less accurate results when adding 300 pixels rather than 200 images. One reason for this issue might be the fact that when increasing the added pixels, the probability of part of the cropped version of image 2 being outside of the camera image increases. This naturally yields a lower correlation as intrinsically uncorrelated information is added. Figure 28 clearly

shows that when keeping the correlation threshold constant and progressively increasing the number of pixels added, the accuracy of the heuristic scheme decreases again after reaching a maximum precisely due to this effect. The accuracy of the overall heuristic method, on the other hand, increases as the infeasible results produced by the heuristic scheme in these cases trigger a full search of image 2 which eventually produced an accurate estimate. This effect is particularly strong for low correlation thresholds as using high correlation thresholds suppresses the false-positive identification of inaccurate CBHs.

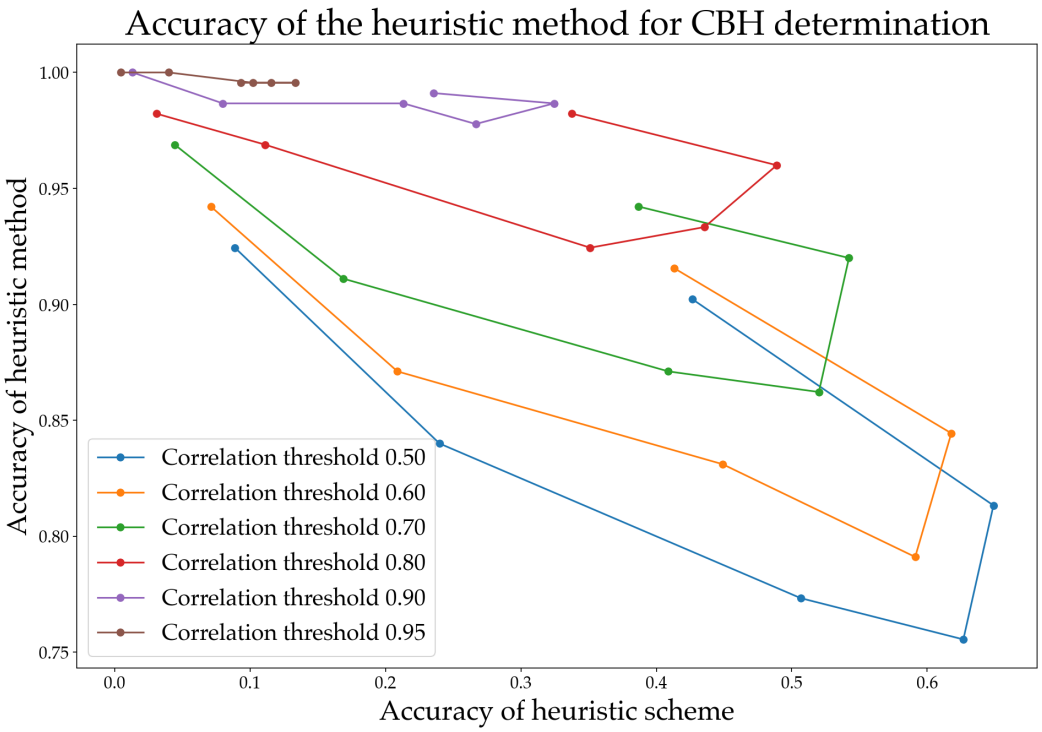

Figure 28. A comparison heuristic scheme for different correlation thresholds versus the full heuristic method. For each threshold, the data points show different numbers of pixels added to the cloud block in image 2.

Overall, these results indicate that both the additional pixels and the correlation threshold should be chosen in a medium range, with too low or too large values being detrimental to either accuracy or computation time. This last point is corroborated by Figure 29: A clear downward-sloping trend can be discerned, implying that higher accuracy also leads to less computing time saved and vice versa. An optimum appears to be reached when adding 200

pixels to the cloud block in image two and using a correlation threshold of 0.8: In this case, the heuristic method produces the same results as the full method in 96% of all cases, but comes with rather substantial computational savings of 36%.

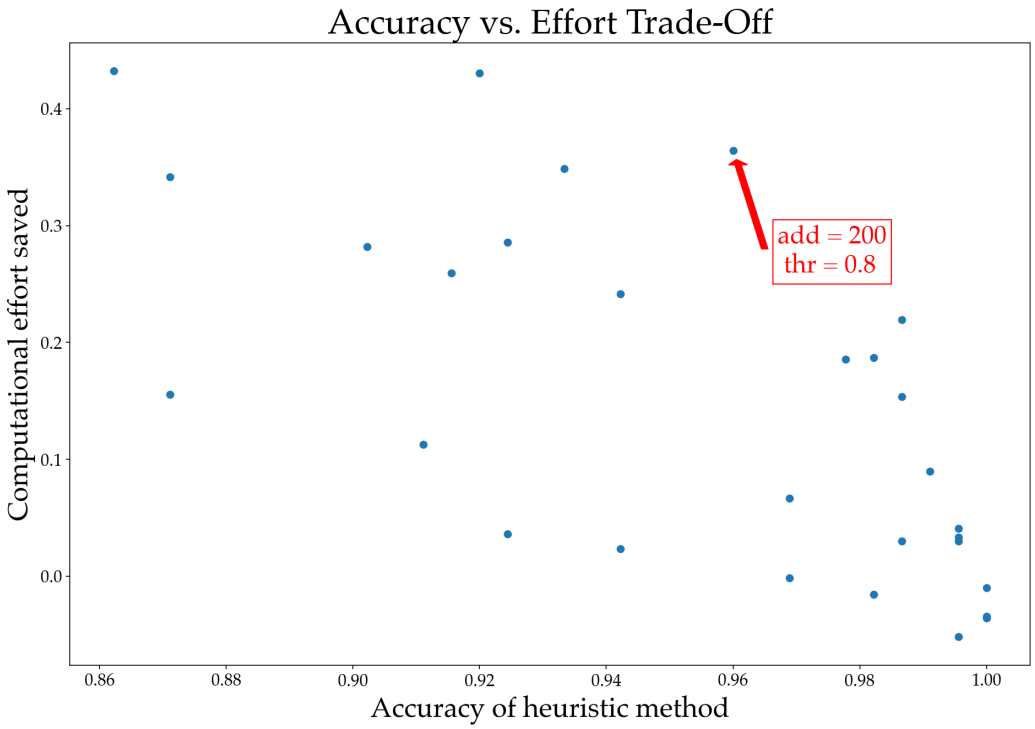

Figure 29. The trade-off between saving computational power and accuracy when using the heuristic method, for those data points from Table 1 that achieved an accuracy with respect to the full method of at least 0.85.

The goal of this part of the research project twofold: Firstly, to establish whether it is possible to use heuristic considerations - assuming a prior CBH for each cloud block based on the previous cloud block's CBH - to reduce computing energy required for CBH estimations in the context of solar nowcasting. Secondly, a working flow was proposed that should be able to accommodate this heuristic method in the context of a future eight-camera set-up to be used for solar nowcasting at the campus of Utrecht University. Based on the results of trying out the heuristic method on an existing pair of sky images, it is concluded that it is indeed possible to implement a heuristic scheme that results in less computation time (and consequently less energy consumption) for CBH estimation based on sky images taken by two imagers. Two important

parameters were established: 1) the number of pixels added at each side of the template shape, and 2) the minimum correlation threshold resulting from the template process required to accept the CBH result. The above results indicate the optimum values of these parameters: a threshold value of around 0.8 and about 200 pixels added at each side. For these intermediate values, very little accuracy was lost when implementing the overall method using full template matching as a fallback when the heuristic scheme did not yield a satisfactory result, while still reducing the overall computation time by roughly 30%.

Influence of Camera Height

In the process of determining Cloud Base Height (CBH), a common assumption made is that the cameras used for capturing sky images are positioned at the same elevation. This assumption simplifies the calculations but does not account for scenarios where the cameras are at differing heights. The potential impact of such elevation differences was theoretically examined previously and can be empirically evaluated by incorporating these height disparities into the *CBH* calculation process and observing any resultant variations in the CBH data.

To quantitatively measure the significance of camera height discrepancies on *CBH* accuracy, we introduce the relative CBH deviation formula:

$$CBH_{dev} = \frac{CBH_{mis} - CBH}{CBH}$$

Here, CBH_{mis} represents the erroneous CBH value derived under the assumption of equal camera elevation, while CBH stands for the actual CBH value. We anticipate that CBH_{dev} will predominantly depend on the height difference between the cameras and the true *CBH* itself. This analytical approach allows us to assess the extent to which varying camera elevations can influence the precision of CBH estimations, a factor that is particularly relevant in complex topographical settings or when utilizing cameras at different buildings or structures.

Results are shown in Figure 30. The relative *CBH* error increases for larger camera height differences, and is inversely related to the actual *CBH*.

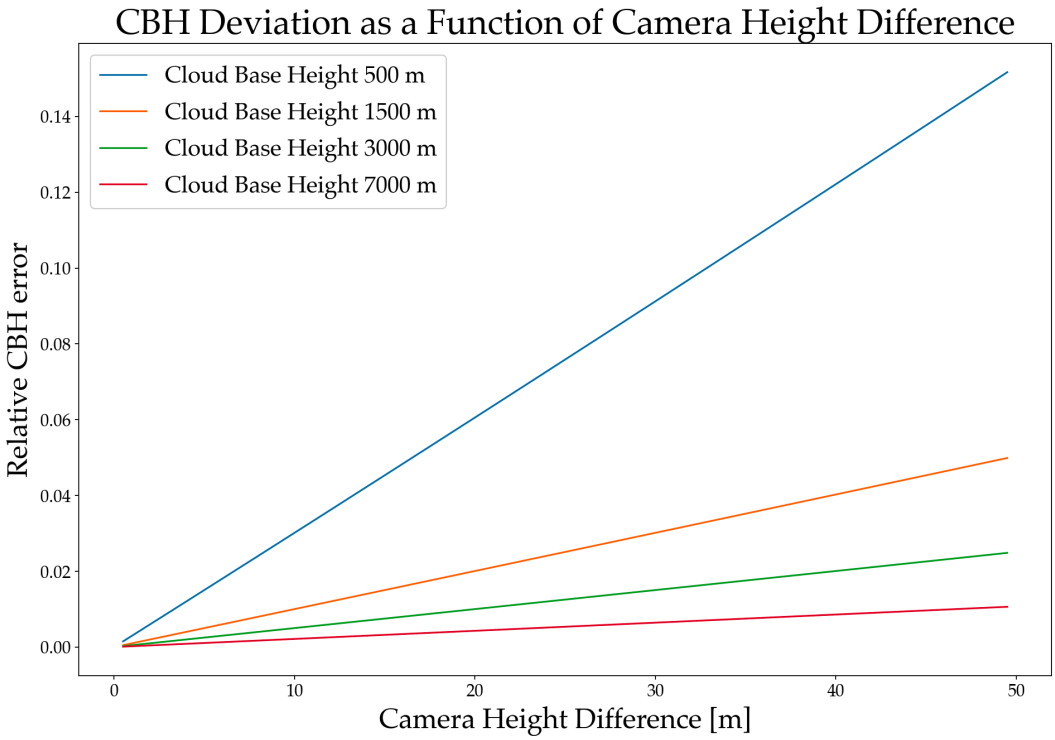

Figure 30. The influence of the camera height difference on the relative CBH error for different CBH.

The research presented in this section underscores that epipolar geometry and stereographic imaging can effectively determine *CBH* and can be further enhanced with heuristic methods to reduce computaional effort, which is especially beneficial in multi-camera configurations. However, the method needs further testing under various real-life conditions.

4. Discussion

In this project, we focused on advancing short-term solar forecasting by utilizing an all-sky imaging network. Our methodology involved strategically deploying all-sky imagers to analyze cloud movement, thereby predicting its impact on solar irradiance. This approach was instrumental in refining cloud detection processes, with the SLIC algorithm proving to be particularly effective across diverse weather conditions. Additionally, we successfully implemented a heuristic method for Cloud Base Height estimation in a multi-camera setup. This innovative approach significantly reduced computational time, optimizing the process of CBH calculation. Moreover, the development of a machine learning algorithm for creating accurate irradiance maps showed promise, particularly for longer forecast periods, despite some challenges related to data quality and dataset size. Overcoming these limitations is expected to lead to further enhancements in forecasting accuracy. Collectively, the findings from our study demonstrate the potential of combining advanced machine learning techniques with comprehensive cloud data analysis. This integrated approach is a crucial step forward in improving the operational efficiency of photovoltaic power systems, crucially adapting to the dynamic nature of solar irradiance, and marking a significant advancement in solar energy forecasting.

The SolFaSi project was an ambitious project with innovative and challenging objectives given the available budget. It was even more challenging due to Covid-related restrictions which did not allow us to take the necessary steps to install equipment. At the end of the project, the envisaged camera set-up has been realized, but data acquisition results are minimal. Therefore, other data sets available due to our participation in the IEA-PVPS Task16 as well as from another site managed by KNMI have been used to develop image analysis and forecasting algorithms.

Given the limited data collected, no effort could be made regarding potential business plan development. However, on the basis of our dissemination activities and the world-wide attention for sky-image based forecasting, a clear business is evident. The value of forecasting

has not been assessed, while others already have shown that certain value is present depending on the stakeholder involved.

5. Dissemination

Dissemination activities have aimed to promote non-confidential results obtained within the project as swiftly and effectively as possible for the benefit of the whole (scientific) community and to avoid duplication of R&D efforts. In particular, our forecasting results have been shared with experts of the IEA-PVPS Task 16 ("Reliability and Performance of Photovoltaic Systems") group, and we have participated in a benchmark study in which various sky-imagers and forecast software was compared.

Published papers

N.Y. Hendrikx, K. Barhmi, L.R. Visser, T.A. de Bruin, M. Pó, A.A. Salah, W.G.J.H.M. van Sark, *All sky imaging based short-term solar irradiance forecasting with Long Short-Term Memory networks*, Solar Energy 272 (2024) 112463. (doi:10.1016/j.solener.2024.112463)

K. Barhmi, C. Heynen, S. Golroodbari, W. van Sark, *A Review of Solar Forecasting Techniques and the Role of Artificial Intelligence*, Solar 4 (2024) 99 – 135. (doi:10.3390/solar4010005)

S.-A. Logothetis, V. Salamalikis, S. Wilbert, J. Remund, L. Zarzalejo, Y. Xie, B. Nourie, E. Ntavelise, J. Nou, N. Hendrikx, L. Visser, M. Sengupta, M. Pó, R. Chauvin, S. Grieu, N. Blum, W. van Sark, A. Kazantzidis, *Benchmarking of solar irradiance nowcast performance derived from all-sky imagers*, Renewable Energy 199 (2022) 246 - 261. (doi:10.1016/j.renene.2022.08.127)

S.-A. Logothetis, V. Salamalikis, B. Nouri, J. Remund, L.F. Zarzalejo, Y. Xie, S. Wilbert, E. Ntavelis, J. Nou, N. Hendrikx, L. Visser, M. Sengupta, M. Pó, R. Chauvin, S. Grieu, N. Blum, W. van Sark, A. Kazantzidis, *Solar irradiance ramp forecasting based on all-sky imagers*, Energies 15 (2022) 6191. (doi:10.3390/en15176191)

L. Visser, E. Lorenz, D. Heinemann, W. van Sark, *Solar power forecasts*, Chapter 1.11 in W.G.J.H.M. van Sark, V. Fthenakis (Eds.) *Photovoltaic Technology,* Volume 1 in T. Letcher (Ed.) *Comprehensive Renewable Energy 2nd Edition,* Elsevier, United Kingdom, 2022, pp. 213 – 233.

S.-A. Logothetis, V. Salamalikis, S. Wilbert, J. Remund, L. Zarzalejo, Y. Xie, B. Nouri, E. Ntavelis, J. Nou, L. Visser, M. Sengupta, M. Pó, R. Chauvin, S. Grieu, W. van Sark, A. Kazantzidis, A.: *Forecasting of solar irradiance and ramp events with all-sky imagers*, EMS Annual Meeting 2021, EMS Annual Meeting Abstracts, Vol. 18, EMS2021-75, 2021, (doi:10.5194/ems2021-75**)**

Conference contributions

K. Barhmi, S. Mirbagheri Golroodbari, W. van Sark, *Benchmarking of 3D cloud information and detection classification methods for solar nowcasting based on All-Sky Imagers for the city of Utrecht, the Netherlands,* 40th EU PVSEC Lisbon 18-22 September 2023 (poster presentation)

K. Barhmi, S. Mirbagheri Golroodbari, W. van Sark, *3D Cloud information and detection for solar nowcasting based on All-Sky Imagers*, 8th World Conference on Photovoltaic Energy Conversion (WCPEC-8), Milano, Italy 26-30 September 2022 (poster presentation)

S.-A. Logothetis, V. Salamalikis, S. Wilbert, J. Remund, L. Zarzalejo, Y. Xie, B. Nouri, E. Ntavelis, J. Nou, L. Visser, M. Sengupta, M. Pó, R. Chauvin, S. Grieu, W. van Sark, A. Kazantzidis, *Solar irradiance ramp events forecasting based on all-sky imagers*, International Radiation Symposium, 4-8 July 2022, Thessaloniki, Greece (oral presentation)

K. Barhmi, S. Mirbagheri Golroodbari, W. van Sark, *3D Cloud information and detection for solar nowcasting based on All-Sky Imagers*, 29th Young Energy Economists and Engineers Seminar (YEEES), 12-13 May 2022, Ghent, Belgium (poster presentation)

S. Wilbert, A. Kazantzidis, J. Remund, L. Zarzalejo, V. Salamalik, S. Logothetis, A. Kumler, B. Nouri, E. Ntavelis, J. Nou, L. Visser, M. Sengupta, M. Pó, R. Chauvin, S. Grieu, W. van Sark, *Bewertung und Vergleich von Wolkenkamerasystemen zur Strahlungsvorhersage*, 36. PV-Symposium, Freiburg, Germany, 18-21 May 2021 (oral presentation).

S.-A. Logothetis, V. Salamalikis, S. Wilbert, J. Remund, L. Zarzalejo, Y, Xie, B. Nouri, E. Ntavelis, J. Nou, L. Visser, M. Sengupta, M. Pó, R. Chauvin, S. Grieu, W. van Sark, A. Kazantzidis, *Solar radiation forecasts based on all sky cameras*, ΠΡΟΓΝΩΣΗ ΤΗΣ ΗΛΙΑΚΗΣ ΑΚΤΙΝΟΒΟΛΙΑΣ ΜΕ ΧΡΗΣΗ ALL SKY ΚΑΜΕΡΩΝ, Proceedings 12th National Conference on Renewable Energy Sources 2021 - Institute of Solar Technology, Thessaloniki, Greece, 7-9 April 2021 (oral presentation).

S. Wilbert, A. Kazantzidis, S. Logothetis, V. Salamalikis, J. Remund, L.F. Zarzalejo, B. Nouri, E. Ntavelis, J. Nou, L. Visser, M. Sengupta, M. Pó, N. Blum, R. Chauvin, S. Grieu, T. Schmidt, W. van Sark, Y. Xie (2021) *Bewertung und Vergleich von Wolkenkamerasystemen zur Strahlungsvorhersage.* In: Tagungsband 36. PV-Symposium / BIPV-Forum. PV Symposium, Online, ISBN 978-3-948176-14-3.

Student reports

- Paul Roßteutscher, A heuristic method for cloud base height determination in a multi-camera context, Tailor made course Master Energy Science, Utrecht University, 2023.
- Chris Heynen, Short term solar now casting through the determination of shadow fields using All Sky Cameras, Thesis Master Energy Science, Utrecht University, 2022.
- Niels Hendrikx, Short term solar irradiance time-series forecasting with machine learning, Master Computing Science, Utrecht University, 2020

PR of project and further PR possibilities

The project partners would like to be approached for any further publicity activities and would like to contribute to public activities of the Rijksdienst voor Ondernemend Nederland or the TKI-Urban Energy and are happy to add these insights to the debate about the energy transition in the Netherlands.

References

[1] Dutch New Energy, Solar Trend Rapport 2024, https://www.solarsolutions.nl/trendrapport/

[2] W. Folkerts, W. van Sark, C. de Keizer, W. van Hooff, M. van den Donker, Roadmap PV systemen en toepassingen, 2017.

[3] A. Kaur, L. Nonnenmacher, H.T.C. Pedro, C. F.M. Coimbra, Benefits of solar forecasting for energy imbalance markets, Renewable Energy 86 (2016) 819 – 830.

[4] L.R. Visser, E.M.B. Schuurmans, T.A. AlSkaif, H.A. Fidder, A.M. van Voorden, W.G.J.H.M. van Sark, Regulation strategies for mitigating voltage fluctuations induced by photovoltaic solar systems in an urban low voltage grid, International Journal of Electricial Power and Energy Systems 137 (2022) 107695.

[5] J. Antonanzas, N. Osorio, R. Escobar, R. Urraca, F. J. Martinez-de-Pison, F. Antonanzas-Torres, Review of photovoltaic power forecasting, Solar Energy 136 (2016) 78–111.

[6] P.-J. Alet, V. Efthymiou. G. Graditi, M. Juel, D. Moser, F. Nemac, M. Pierro, E. RIkos, S. Tselepis, G. Yang, Assessing the need for better forecasting and observability of PV, a White Paper by the European Technology & Innovation Platform, Working Group on Grid Integration, 2017.

[7] P. Tzoumanikas, E. Nikitidou, A.F. Bais, A. Kazantzidis, The effect of clouds on surface solar irradiance, based on data from an all-sky imaging system, Renewable Energy 95 (2016) 314 –322.

[8] S. Dev, Y. H. Lee, S. Winkler., Categorization of cloud image patches using an improved texton-based approach., Proceedings IEEE International Conference on Image Processing (ICIP), Québec City, Canada, 2015.

[9] P. Tuominen, M. Tuononen, Cloud detection and movement estimation based on sky camera images using neural networks and the Lucas-Kanade method, AIP Conference Proceedings 1850 (2017) 140020

[10] Y. Ai, Y. Peng, W. Wei, A model of very short-term solar irradiance forecasting based on low- cost sky images, AIP Conference Proceedings 1839 (2017) 020022.

[11] J. Kleissl, Solar energy forecasting and resource assessment. Academic Press, 2013.

[12] F. Barbieri, S. Rajakaruna, A. Ghosh, Very short-term photovoltaic power forecasting with cloud modeling: A review, Renewable and Sustainable Energy Reviews, 75 (2017) 242-263. doi: 10.1016/j.rser.2016.10.068.

[13] B.J. Martins, J.M. Arrais, A. Cerentini, A. von Wangenheim, G.P.R. Neto, S. Mantelli, Segmentation and Classification of Individual Clouds in Images Captured with Horizon-Aimed Cameras for Nowcasting of Solar Irradiance Absorption, American Journal of Climate Change 12 (2023) 628-654. doi: 10.4236/ajcc.2023.124027

[14] P. H. Akwensi, Z. Kang, R. Wang, Hyperspectral image-aided LiDAR point cloud labeling via spatio-spectral feature representation learning, International Journal of Applied Earth Observation and Geoinformation, 120 (2023) 103302. doi: 10.1016/j.jag.2023.103302.

[15] G. Doxani, E. Vermote, J.-C. Roger, F. Gascon, S. Adriaensen, D. Frantz, O. Hagolle, A. Hollstein, G. Kirches, F. Li, J. Louis, A. Mangin, N. Pahlevan, B. Pflug, Q. Vanhellemont, Atmospheric correction inter-comparison exercise, Remote Sensing 10 (2018) 353. doi: 10.3390/rs10020352.

[16] S. Liu, L. Zhang, Z. Zhang, C. Wang, B. Xiao, Automatic cloud detection for all-sky images using superpixel segmentation, IEEE Geoscience and Remote Sensing Letters 12 (2015) 354–358. doi: 10.1109/LGRS.2014.2341291.

[17] Y. Fabel, B. Nouri, S. Wilbert, N. Blum, R. Triebel, M. Hasenbalg, P. Kuhn, L.F. Zarzalejo, R. Pitz-Paal Applying self-supervised learning for semantic cloud segmentation of all-sky images, Atmospheric Measurement Techniques 15 (2022) 797-809. doi: 10.5194/amt-15-797-2022.

[18] R. J. Al-Azawi, Q. S. Al-Jubouri, and Y. A. Mohammed, Enhanced algorithm of superpixel segmentation using simple linear iterative clustering, in Proceedings 12th International Conference on Developments in eSystems Engineering (DeSE) (2019) pp. 160-163. doi: 10.1109/DeSE.2019.00038.

[19] A. Driemel, J. Augustine, K. Behrens, S. Colle, C. Cox, E. Cuevas-Agulló, F. M. Denn, T. Duprat, M. Fukuda, H. Grobe, M. Haeffelin, N. Hyett, O. Ijima, A. Kallis, W. H. Knap, V. Kustov, C. N. Long, D. Longenecker, A. Lupi, M. Maturilli, M. Mimouni, L. Ntsangwane, H. Ogihara, X. Olano, M. Olefs, M. Omori, L. Passamani, E. Bueno Pereira, H. Schmithüsen, S.

Schumacher, R. Sieger, J. Tamlyn, R. Vogt, L. Vuilleumier, X. Xia, A. Ohmura, G. König-Langlo, Baseline Surface Radiation Network (BSRN): structure and data description (1992-2017), Earth System Science Data 10 (2018) 1491-1501.

[20] W. Wu, J. Lin, S. Wang, Y. Li, M. Liu, G. Liu, J. Cai, G. Chen, R. Chen, A novel multiphoton microscopy images segmentation method based on superpixel and watershed, Journal of Biophotonics 10 (2017) 532–541. doi: 10.1002/jbio.201600007.

[21] P. F. Felzenszwalb, D. P. Huttenlocher, Efficient graph-based image segmentation, International Journal of Computer Vision 59 (2004) 167-181, doi: 10.1023/B:VISI.0000022288.19776.77.

[22] D. Haputhanthri, D. De Silva, S. Sierla, D. Alahakoon, R. Nawaratne, A. Jennings, V. Vyatkin, Solar Irradiance Nowcasting for Virtual Power Plants Using Multimodal Long Short-Term Memory Networks, *Frontiers in Energy Research* 9 (2021) 722212. doi: 10.3389/fenrg.2021.722212.

[23] C. W. Chow, B. Urquhart, M. Lave, A. Dominguez, J. Kleissl, J. Shields, B. Washom, Intra-hour forecasting with a total sky imager at the UC San Diego solar energy testbed, *Solar Energy* 85 (2011) 2881-2893. doi: 10.1016/j.solener.2011.08.025.

[24] S. Sun, J. Ernst, A. Sapkota, E. Ritzhaupt-Kleissl, J. Wiles, J. Bamberger, T. Chen, Short term cloud coverage prediction using ground based all sky imager, Proceedings 2014 IEEE International Conference on Smart Grid Communications (SmartGridComm 2014) (2015) 121-126. doi: 10.1109/SmartGridComm.2014.7007633.

[25] CAMS, Copernicus Atmosphere Monitoring Service, https://atmosphere.copernicus.eu

[26] W.F. Holmgren, C.W. Hansen, M.A. Mikofski, pvlib python: a python package for modeling solar energy systems. Journal of Open Source Software, 3 (2018) 884. doi: 10.21105/joss.00884

[27] B. Nouri, S. Wilbert, L. Segura, P. Kuhn, N. Hanrieder, A. Kazantzidis, T. Schmidt, L. Zarzalejo, P. Blanc, R. Pitz-Paal, Determination of cloud transmittance for all sky imager based solar nowcasting, Solar Energy 181 (2019), doi: 10.1016/j.solener.2019.02.004.

[28] P. Kuhn, B. Nouri, S. Wilbert, C. Prahl, N. Kozonek, T. Schmidt, Z. Yasser, L. Ramirez, L. Zarzalejo, A. Meyer, L. Vuilleumier, D. Heinemann, P. Blanc,R. Pitz-Paal, Validation of an all-

sky imager–based nowcasting system for industrial PV plants, Progress in Photovoltaics: Research and Applications 26 (2018) 608–621. doi: 10.1002/pip.2968.

[29] C. L. Fu, H. Y. Cheng, Predicting solar irradiance with all-sky image features via regression, Solar Energy 97 (2013) 537-550. doi: 10.1016/j.solener.2013.09.016.

[30] Y. Chu, H. T. C. Pedro, C. F. M. Coimbra, Hybrid intra-hour DNI forecasts with sky image processing enhanced by stochastic learning, Solar Energy 98 (2013) 592–603. doi: 10.1016/j.solener/2013.10.020.

[31] Z. Zhen, F. Wang, Y. Sun, Z. Mi, C. Liu, B. Wang, J. Lu, SVM based cloud classification model using total sky images for PV power forecasting, Proceedings 2015 IEEE Power and Energy Society Innovative Smart Grid Technologies Conference (ISGT 2015) (2015). doi: 10.1109/ISGT.2015.7131784.

[32] Z. Peng, D. Yu, D. Huang, J. Heiser, S. Yoo, P. Kalb, 3D cloud detection and tracking system for solar forecast using multiple sky imagers, Solar Energy 118 (2015) 496-519, doi: 10.1016/j.solener.2015.05.037.

[33] A. Heinle, A. Macke, A. Srivastav, Automatic cloud classification of whole sky images, Atmospheric Measurement Techniques 3 (2010) 557–567, doi: 10.5194/amt-3-557-2010

[34] M. Singh, M. Glennen, Automated ground-based cloud recognition, Pattern Analysis and Applications 8 (2005) 258–271, doi: 10.1007/s10044-005-0007-5.

[35] S. Dev, B. Wen, Y. H. Lee, S. Winkler, Ground-based image analysis: A tutorial on machine-learning techniques and applications, IEEE Geoscience and Remote Sensing Magazine 4 (2016) 79 – 93, doi: 10.1109/MGRS.2015.2510448.

[36] C. Voyant, G. Notton, Solar irradiation nowcasting by stochastic persistence: A new parsimonious, simple and efficient forecasting tool, Renewable and Sustainable Energy Reviews 92 (2018), 343-352, doi: 10.1016/j.rser.2018.04.116.

[37] G. Wang, B. Kurtz, J. Kleissl, Cloud base height from sky imager and cloud speed sensor, Solar Energy 131 (2016) 208-221, doi: 10.1016/j.solener.2016.02.027.

[38] T. Schmidt, J. Kalisch, E. Lorenz, D. Heinemann, Evaluating the spatio-temporal performance of sky-imager-based solar irradiance analysis and forecasts, Atmospheric Chemistry and Physics 16 (2016) 3399–3412, doi: 10.5194/acp-16-3399-2016.

[39] Y.-J. Noh, J.M. Forsythe, S.D. Miller, C.J. Seaman, Y. Li, A.K. Heidinger, D.T. Lindsey, M.A. Rogers, P.T. Partain, Cloud-base height estimation from VIIRS. part II: A statistical algorithm based on A-train satellite data, Journal Atmospheric Ocean Technology 34 (2017) 585-598, doi: 10.1175/JTECH-D-16-0110.1.

[40] M. Costa-Surós, J. Calbó, J. A. González, J. Martin-Vide, Behavior of cloud base height from ceilometer measurements, Atmospheric Research 127 (2013) 64-76, doi: 10.1016/j.atmosres.2013.02.005.

[41] L. Liu, X. J. Sun, X. C. Liu, T. C. Gao, S. J. Zhao, Comparison of cloud base height derived from a ground-based infrared cloud measurement and two ceilometers, Advances in Meteorology, 2015 (2015) 853861, doi: 10.1155/2015/853861.

[42] V. Fung, J. L. Bosch, S. W. Roberts, J. Kleissl, Cloud shadow speed sensor, *Atmospheric Measurement Techniques* 7 (2014) 1693-1700, doi: 10.5194/amt-7-1693-2014.

[43] D. Nguyen, J. Kleissl, Stereographic methods for cloud base height determination using two sky imagers, Solar Energy 107 (2014) 496-509, doi: 10.1016/j.solener.2014.05.005.

[44] Z. Zhang, R. Deriche, O. Faugeras, Q.-T. Luong, A robust technique for matching two uncalibrated images through the recovery of the unknown epipolar geometry. Artificial Intelligence 78 (1995) 87–119.

[45] X. Armangué, J. Salvi, Overall view regarding fundamental matrix estimation. Image and Vision Computing 21 (2003) 205–220.

[46] Bradski, G. (2000). The OpenCV Library. Dr Dobb's Journal of Software Tools 25 (2000) 120-125.